

Doctoral Thesis

Enhanced Fidelity of Monte Carlo Coupled  
Multi-Physics Simulations for Light Water Reactors

Muhammad Makrus Imron

Department of Nuclear Engineering

Ulsan National Institute of Science and Technology

2025

# Enhanced Fidelity of Monte Carlo Coupled Multi-Physics Simulations for Light Water Reactors

Muhammad Makrus Imron

Department of Nuclear Engineering

Ulsan National Institute of Science and Technology

## Abstract

This study presents a framework to enhance the fidelity of typical Monte Carlo (MC) coupled multi-physics simulations for Light Water Reactors (LWRs) through two key improvements. First, the introduction of multi-physics simulations with spatially continuous material properties using the Functional Expansion Tally (FET) combined with delta-tracking. Second, the incorporation of on-the-fly thermal expansion of reactor core components during MC particle tracking. In direct multi-physics coupled MC simulations, the use of spatially continuous material properties is particularly crucial to accurately modeling spatial self-shielding effects, which depend on smooth intra-fuel-pellet temperature distributions. The significant reduction in discretization also preserves the MC method's advantage in handling continuous geometry. Additionally, modeling thermal expansion is essential because the geometric data of reactor components is typically provided at room temperature, while reactors operate at much higher temperatures. Numerical experiments are conducted to assess the applicability and advantages of the proposed multi-physics framework across a range of reactor core problems, from two-dimensional pin-cell to whole-core reactor problems.

The incorporation of spatially continuous material properties produces solutions that asymptotically converge to those from conventional cell-based discretized simulations with infinitesimally small cells as demonstrated in the two-dimensional pin-cell problem. Similar outcomes are observed in three-dimensional pin cell and assembly problems, where the continuous representation of material properties results in more accurate solutions for both eigenvalue and axial power distributions, compared to the conventional cell-based discretization method. In typical whole-core LWR problems, the proposed method reproduces high-fidelity solutions for both eigenvalue and pin powers, while reducing simulation times by around threefold and requiring 80% less memory than the traditional cell-based discretization using very small cells.

Whereas the numerical results for on-the-fly thermal expansion demonstrate that the observed trends in reactivity differences due to thermal expansion for varying boron concentrations and fuel temperatures align with previous studies. Additionally, the calculated Isothermal Temperature Coefficients (ITC) show improvement when thermal expansion is considered. Using core-averaged temperatures for expansion provides fairly accurate results, but employing local temperatures at pin levels can enhance accuracy further. Moreover, incorporating thermal expansion also improves solutions for depletion problems, especially at high power and high fuel burnup. These findings suggest that integrating the proposed framework into reactor modeling can significantly enhance simulation fidelity. Therefore, the framework has the potential to be incorporated into future Monte Carlo production codes to meet the growing demands for improved reactor safety.



## Contents

I	Introduction . . . . .	1
1.1	Spatial Resolution . . . . .	1
1.2	Thermal Expansion . . . . .	3
1.3	Scope and Objectives . . . . .	5
1.4	Thesis Outline . . . . .	5
II	Spatially Continuous Material Properties . . . . .	7
2.1	Functional Expansion Tally . . . . .	7
2.2	Polynomials Calculation . . . . .	8
2.3	Overcoming Discontinuities . . . . .	11
2.4	Variance Estimation . . . . .	14
2.5	Delta-Tracking . . . . .	14
2.6	Majorant Cross-Section Computation . . . . .	16
2.7	Calculation Flow . . . . .	16
III	Thermal Expansion . . . . .	21
3.1	Theory . . . . .	21
3.2	Thermal Expansion Coefficients . . . . .	21
3.3	Thermal-Hydraulics Coupling . . . . .	22

3.4	On-The-Fly Thermal Expansion . . . . .	23
3.5	Calculation Flow . . . . .	25
IV	Numerical Results . . . . .	27
4.1	Benchmark Description . . . . .	27
4.2	Spatially Continuous Material Properties . . . . .	27
4.2.1	Two-dimensional Pin-cell Problem . . . . .	29
4.2.2	Three-dimensional Pin-cell Problem . . . . .	30
4.2.3	Three-dimensional Assembly Problem . . . . .	32
4.2.4	Three-dimensional Assembly Problem with Neutron Absorbers . . . . .	36
4.2.5	Whole-core Reactor Problem . . . . .	36
4.3	Thermal Expansion . . . . .	43
4.3.1	Small Lattice Problem . . . . .	43
4.3.2	Assembly Problem . . . . .	44
4.3.3	Whole-core Reactor Problem . . . . .	44
4.3.4	Isothermal Temperature Coefficient . . . . .	46
4.3.5	Whole-core Reactor Depletion using Restart Calculations . . . . .	48
4.4	Combined Framework . . . . .	49
4.4.1	Assembly Problem . . . . .	49
4.4.2	Whole-core Reactor Problem . . . . .	49
V	Conclusion . . . . .	52
5.1	Thesis Summary . . . . .	52
5.2	Future Work . . . . .	53
	References . . . . .	55
	Acknowledgements . . . . .	59

## List of Figures

Figure 1:	Axial view of a typical Monte Carlo geometry model.	2
Figure 2:	The two-step methodology for reactor calculations.	4
Figure 3:	Zernike polynomial orders zero through four	9
Figure 4:	First few orders of Fourier-Bessel series and the radial parts of Zernike polynomials.	11
Figure 5:	Zernike and Fourier-Bessel expansions to approximate function $f(r) = r^2 - 1$ .	12
Figure 6:	Zernike and Fourier-Bessel expansions to approximate function $f(r) = r^2$ .	12
Figure 7:	Comparisons of axial power from mesh tally and FET.	13
Figure 8:	Percent error in axial power from FET without the use of piecewise expansions.	13
Figure 9:	Percent error in axial power from FET with the use of piecewise expansions.	14
Figure 10:	Comparison of majorant microscopic XS of U-238	17
Figure 11:	Comparison of majorant macroscopic XS	17
Figure 12:	Calculation flow of the proposed framework.	19
Figure 13:	Calculation flow to calculate macroscopic cross section	20
Figure 14:	Flow chart of MCS-TH1D coupling interface.	23
Figure 15:	Flow chart of MCS-CTF coupling interface.	24
Figure 16:	The radial expansion of fuel pellet and cladding.	25
Figure 17:	Calculation of geometrical changes due to thermal expansion.	26

Figure 18: On-the-fly thermal expansion during neutron tracking. . . . .	26
Figure 19: Fuel assembly radial layout. . . . .	28
Figure 20: Fuel rod radial layout. . . . .	28
Figure 21: VERA benchmark core configuration and control rods layout. . . . .	28
Figure 22: Radial fuel temperature distribution for two-dimensional pin-cell problem. . . . .	30
Figure 23: Normalized absorption and fission rates . . . . .	31
Figure 24: Extrapolated $k_{inf}$ for two-dimensional pin cell problem. . . . .	31
Figure 25: Normalized axial power, fuel temperature, and coolant density . . . . .	33
Figure 26: Axial power percentage differences of the FET case . . . . .	34
Figure 27: Radial and axial geometries of the three-dimensional assembly problem . . . . .	34
Figure 28: Pin powers comparisons for three-dimensional assembly problem. . . . .	35
Figure 29: Detailed whole-core reactor geometry modelling in MCS. . . . .	37
Figure 30: Assembly powers comparison between FET and E3 cases. . . . .	40
Figure 31: Axial power comparison for the whole-core problem. . . . .	40
Figure 32: Normalized radial pin-power densities of the FET case for the whole-core problems	41
Figure 33: Three-dimensional view of radially pin-averaged coolant and fuel temperatures .	41
Figure 34: Small lattice problem geometry. . . . .	43
Figure 35: Radial pin-power errors distributions relative to the pin-averaged case . . . . .	47

## List of Tables

Table 1:	Key differences between this work and Ellis' work.	3
Table 2:	CPU time for calculating the radial components of the Zernike polynomials	10
Table 3:	Thermal expansion coefficients used in this study.	22
Table 4:	Two-dimensional pin-cell problem infinite multiplication factors.	29
Table 5:	Calculation results for three-dimensional pin-cell problem.	32
Table 6:	Calculation results for three-dimensional assembly problem.	35
Table 7:	Calculation results for assembly problem with neutron absorbers.	38
Table 8:	Calculation results for whole-core problem.	39
Table 9:	Calculation results for FET cases utilizing different orders of Zernike and Legendre polynomials.	39
Table 10:	Small lattice problems infinite multiplication factors.	44
Table 11:	Assembly reactivity differences for various boron concentrations.	45
Table 12:	Assembly reactivity differences for different fuel enrichments.	45
Table 13:	Whole-core problem eigenvalues and pin-power power errors.	45
Table 14:	Calculated ITCs compared with the measured value.	46
Table 15:	Critical boron concentrations for depletion problem.	48
Table 16:	Calculation results for the assembly problem using combined framework.	50
Table 17:	CBC results for the whole-core problem using combined framework.	50

Table 18: Eigenvalue results for the whole-core problem using combined framework. . . . 50

# I Introduction

Over the past five decades, advancements in modern computing have enabled direct whole-core Monte Carlo (MC) coupled multi-physics simulations for large-scale Light Water Reactors (LWRs). In this approach, the multi-physics coupling between MC codes and thermal-hydraulic (TH) solvers is accomplished at the pin-by-pin level. Numerous examples of these reactor multi-physics simulations can be found in the literature [1–3], and they had demonstrated that such simulations are practically feasible for academic and research purposes. The results from such reactor multi-physics simulations have shown improved accuracy when compared to measured data and are often used as reference solutions for lower-order deterministic codes. However, according to Smith and Forget [4], there are still many important aspects of LWR simulations that must be incorporated to produce truly high-fidelity analysis tools.

While the work of Smith and Forget highlights many aspects to improve the fidelity of reactor calculations, this thesis attempts to solve two issues. First, inadequate spatial resolution, such as the improper modeling of radial temperature variations in fuel pellets, which is essential for accurately modeling spatial self-shielding effects [4, 5]. Second, thermal expansion of the reactor core materials, which is often neglected in typical direct whole-core MC coupled multi-physics simulations. The subsequent subsections, 1.1 and 1.2, will discuss each of these aspects in detail. Additionally, a literature review for each aspect is described in those subsections.

## 1.1 Spatial Resolution

One of the main advantages of the MC methodology is its ability to handle continuous geometry within a single material. However, when conducting MC multi-physics reactor simulations, it is necessary to discretize the problem domain into smaller cells, even within the same material. The material properties, such as fuel temperature, moderator density, and the isotopic composition of materials diluted in the moderator, are assumed to be uniform within each cell. This discretization is essential for achieving adequate spatial resolution and accurately modeling variations in material properties.

Figure 1 shows the axial view of a typical MC geometry model for a single fuel pin. The actual geometry consists of the fuel, gap, cladding, and coolant, as illustrated in Figure 1a. For multi-physics simulations, this geometry must be discretized into several cells both radially and axially, as shown in Figure 1b, even though the actual geometry is relatively simple.

Although high spatial resolution can be achieved by discretizing the problem domain into smaller cells, this extra discretization, however, can hinder MC particle tracking. This occurs because the cross-sections must be reconstructed each time a particle crosses a cell boundary. Additionally, the routine that determines a particle’s location within a cell slows down due to the increased number of cells and must be called more frequently. Moreover, this introduces a significant memory burden, as the data for numerous cells must be stored during the simulation. Consequently, this additional discretization in multi-physics simulations reduces the efficiency of the MC method in handling continuous geometry.

Few methods have been developed to address this issue. One of such method is Localized Delta Tracking (LTD) [5], which solves radial heat conduction within the fuel pellet using polynomial fitting.

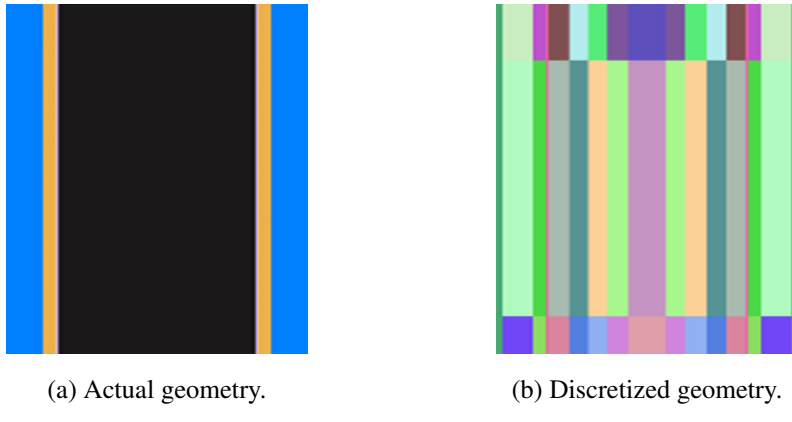


Figure 1. Axial view of a typical Monte Carlo geometry model.

This approach allows for the determination of continuously varying radial fuel temperatures. By using LTD within the fuel pellet, MC multi-physics coupling can be achieved without requiring explicit radial discretization of the fuel pellet. However, LTD is limited to handling continuously varying fuel temperatures only in the radial direction. In the axial direction, traditional discretization of the problem domain is still necessary.

Another study by Leppänen [6] modeled nonuniform density distributions using the Serpent 2 MC Code. In this study, he performed MC multi-physics coupling with continuous moderator density combined with the rejection sampling methodology within a single material region. The application considered in this study is related to the continuously varying distribution of coolant density or void fraction along the flow channel of a nuclear fuel assembly. However, this work did not account for variations in temperature and isotopic composition of the material diluted in the moderator, such as boron.

One notable effort was made by Ellis [7], who employed the Functional Expansion Tally (FET) method [8, 9] to achieve continuous representations of power. After multi-physics feedback calculations, the resulting continuous fuel pellet temperature and coolant density were also modeled using functional expansions. To facilitate MC particle tracking in a continuous medium, a modified version of Continuously Varying Material Tracking (CVMT) [10] was developed. These two methods were integrated to perform MC multi-physics simulations with continuously varying materials.

While Ellis' work and the work presented in this thesis may appear similar, they exhibit several key differences. Firstly, this work successfully develops a technique for calculating the majorant cross-section in a continuous medium, which facilitates delta-tracking and serves as an alternative to CVMT. The use of CVMT introduces complexity by necessitating neutron path integration during particle tracking, thus increasing computational loads. Secondly, this work uses spatial interpolation using a nearly continuous mesh to represent continuous material properties, as opposed to employing FET. This approach reduces the computational burden as it involves fewer arithmetic operations than calculating a complete set of polynomials required by FET. Additionally, the use of spatial interpolation allows that the polynomials are only calculated during physical collisions in delta-tracking method for tallying FET coefficients. Thirdly, this work introduces an efficient method [11] to calculate Zernike polynomials re-

Table 1. Key differences between this work and Ellis' work.

Aspects	This work	Ellis' work	Remarks
Particle-tracking method	Delta-tracking	CVMT	<ul style="list-style-type: none"> <li>• Delta-tracking was not used in the Ellis' work because the difficulty in determining majorant XS.</li> <li>• CVMT adds the complexity of neutron path integration during particle tracking.</li> </ul>
Material properties (i.e., temperature and density) representation	Spatial interpolation using nearly continuous mesh	FET	<ul style="list-style-type: none"> <li>• Spatial interpolation involves fewer arithmetic operations.</li> <li>• Polynomials are only calculated when the collisions are physical.</li> </ul>
Zernike polynomials calculations	Uses recursive formula	Uses conventional formula	Marks the first implementation in FET.
Discretization	Material-wise	Needs discretization when there are spacer grids	This work does not explicit discretization when there are spacer grids.
Scalability	Whole-core level	Assembly level	
Speedup (pin-cell problem)	4.5 times faster	1.7 times faster	

cursively that marks the first implementation in FET. These distinctions, among others, are summarized in Table 1.

## 1.2 Thermal Expansion

Thermal expansion (TE) significantly impacts reactor physics modeling, not only for fast reactors but also, to some extent, for LWRs. That is because the reactor design information is typically provided at room temperature, while the actual reactor core operates at much higher temperatures. For instance, at full power, the nominal fuel temperature is around 900 K, and the coolant temperature is approximately 580 K. This substantial temperature difference causes thermal expansion of all components within the reactor vessel. For example, the core plate expands radially, which increases the assembly pitch. The grid spacers within an assembly also expand, altering the pin pitch within the lattice. Additionally, both the fuel pellet and the fuel rod cladding expand in radial and axial directions [12].

Thermal expansion modeling has long been incorporated into the industry's best-practice two-step

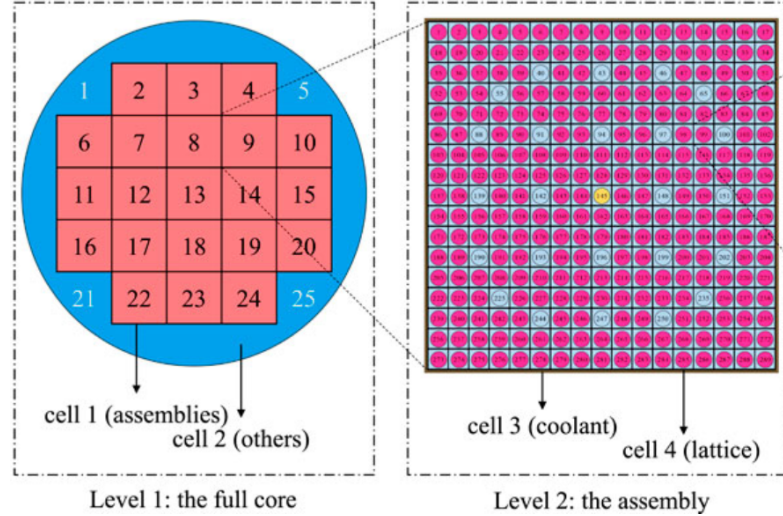


Figure 2. The two-step methodology for reactor calculations. Adapted from [13].

methodology for LWR analysis. The two-step methodology involves lattice physics calculations at the assembly level at which the material is homogenized as illustrated in Figure 2. In this approach, thermal expansion is accounted for during lattice physics calculations to generate the multi-group cross sections for specific operating reactor temperatures. However, direct MC coupled multi-physics simulations present a challenge: local temperature variations are determined from thermal-hydraulic feedback, and they are not known *a priori*. Additionally, these temperatures are typically non-uniform within the reactor core.

To address this challenge, typical TE modeling in direct coupled multi-physics simulations is often achieved by manually adjusting input files to uniformly expand the reactor core geometry and modify material densities. This method typically uses core-averaged nominal temperatures, as demonstrated by Palmtag et al. [12]. In Palmtag's work, thermal expansion was implemented by processing XML input files for the Consortium for Advanced Simulation of LWRs (CASL) core simulator code, VERA-CS, to uniformly adjust core dimensions and material densities. This process is accomplished by VERAIn ASCII input preprocessor. However, the VERAIn ASCII input preprocessor only allows thermal expansion at a pre-set, uniform temperature, typically the core-averaged temperature.

Other studies [14–16] have implemented thermal expansion using thermo-mechanical solvers in Computational Fluid Dynamics (CFD) codes such as OpenFOAM or ANSYS. Generally, these works employed a neutronic solver to obtain power, followed by a CFD code as the TH solver and a mechanical solver to perform material deformation due to temperature changes. However, due to their reliance on direct CFD simulations, these approaches are likely suitable only for small cores, like those in heat pipe or modular reactors. The computational requirements for this method would be exponentially more expensive for larger cores.

Another noteworthy study on reactor simulations with thermal expansion modeling is the work conducted by Idaho National Laboratory [17]. In this study, they modeled feedback mechanisms that include Doppler effects, radial expansion due to the displacement of the support plate, and axial expansion from

the displacement of fuel pins for Unprotected Loss of Flow (ULOF) transient simulations in typical sodium fast reactors. A 2D BISON thermomechanical model of the 316 stainless steel support plate was used to simulate mesh displacement and its effect on the core assembly pitch. Meanwhile, fuel expansion was modeled using a 3D BISON thermomechanical model of the fuel pins. To integrate these models into a multi-physics simulation, they employed the MOOSE multi-app system [18], with Griffin, the neutronics solver, serving as the main application.

### 1.3 Scope and Objectives

The objective of this study is to present a framework that enhances the fidelity of typical MC coupled multi-physics simulations for LWRs, through two key improvements. First, the introduction of multi-physics simulations with spatially continuous material properties [19] to address the spatial resolution issue discussed earlier. Second, the incorporation of on-the-fly thermal expansion of reactor core components during MC particle tracking [20].

MC coupled multi-physics simulations with spatially continuous material properties are achieved using FET in combination with delta-tracking. By using delta-tracking instead of CVMT, the complexity of neutron path integration during particle tracking is eliminated. The proposed method is non-intrusive to the thermal-hydraulic (TH) solver, meaning no modifications are required to the TH solver module. This work also adopts an efficient approach from [11] for constructing Zernike polynomials, marking the first use of this method in the application of FET for reactor core simulations.

While the incorporation of thermal expansion is achieved through on-the-fly thermal expansion in MC coupled multi-physics reactor simulations. This method dynamically expands the reactor geometry during particle tracking, enhancing accuracy by using local temperatures, such as pin-averaged or assembly-averaged temperatures, rather than core averaged temperatures. Additionally, as will be shown later in the numerical results section, this approach introduces negligible computational overhead.

This study is limited to static MC coupled multi-physics problems for LWRs. Although the proposed multi-physics framework is applicable to general LWRs, this study specifically focuses on Westinghouse-type Pressurized Water Reactors (PWRs). Additionally, it is restricted to fresh core reactor problems and does not consider depletion or multi-cycle reactor problems. Although spatially continuous depletion is a topic worth exploring, this will be left for future work.

The proposed multi-physics framework in this study has been implemented in the MCS code [21] to evaluate its applicability and effectiveness across a range of reactor core problems, from two-dimensional pin-cell models to realistic whole-core reactor problems. MCS is a neutron/photon transport code developed at the Ulsan National Institute of Science and Technology (UNIST), with capabilities for multi-physics and multi-cycle reactor analysis [22–24].

### 1.4 Thesis Outline

This thesis is structured into five sections. Section I provides the background and motivations for the study. Sections II and III discuss the theoretical framework for MC coupled multi-physics simulations

with spatially continuous materials and on-the-fly thermal expansion, respectively. The numerical results are presented and discussed in Section IV, which is divided into four major subsections: subsection 4.1 describes the benchmark problem used to evaluate the proposed framework; subsection 4.2 discusses the solutions from multi-physics simulations with spatially continuous material properties; subsection 4.3 focuses on solutions from on-the-fly thermal expansion; and subsection 4.4 presents solutions combining both methodologies. Finally, Section V concludes this thesis and outlines potential future research directions based on the findings.

## II Spatially Continuous Material Properties

This section provides the theoretical background for Monte Carlo (MC) coupled multi-physics simulations with spatially continuous materials. Section 2.1 explains the theory behind Functional Expansion Tally (FET), followed by the calculation of the polynomial basis required for FET in section 2.2 and how to overcome function discontinuities in section 2.3. The variance estimation of the reconstructed power is briefly discussed in section 2.4. The use of delta-tracking for spatially continuous materials is described in section 2.5, along with the computation of majorant cross-sections in section 2.6. Finally, section 2.7 summarizes the calculation flow for MC coupled multi-physics simulations with spatially continuous materials.

### 2.1 Functional Expansion Tally

In the FET methodology [7,9], the actual power shape solution is approximated through a truncated linear combination of polynomials, with MC tallies used to calculate the coefficients of these polynomials. Therefore, the spatially continuous power distribution can be approximated using FET by expanding the tally quantity into a linear combination of polynomials  $\psi(\vec{\xi})$ , as shown below:

$$f(\vec{\xi}) = \sum_{n=0}^{\infty} \bar{a}_n k_n \psi_n(\vec{\xi}), \quad (1)$$

$$\bar{a}_n = \langle f, \psi_n \rangle = \int_{\Gamma} f(\vec{\xi}) \psi_n(\vec{\xi}) \rho(\vec{\xi}) d\vec{\xi}. \quad (2)$$

Here,  $\bar{a}_n$  represents the expansion coefficients,  $\vec{\xi}$  denotes the neutron phase space comprising  $(\vec{r}, \hat{\Omega}, E)$ , and  $k_n$  is the normalization constant, which can be determined based on the chosen polynomial basis set that can be expressed as:

$$k_n = \frac{1}{\|\psi_n\|^2}, \quad (3)$$

where

$$\|\psi_n\|^2 = \int_{\Gamma} \psi_n^2(\vec{\xi}) \rho(\vec{\xi}) d\vec{\xi}. \quad (4)$$

Lastly, the  $\rho(\vec{\xi})$  is the weighting function that shall be both complete and orthogonal with respect to  $\psi_n(\vec{\xi})$ .

Fortunately, the integrals required to obtain the expansion coefficients in Eq. 2 can be easily calculated in MC simulations using both analog and collision-based estimators. The unbiased collision-based estimator for the coefficients  $\bar{a}_n$ , used to reconstruct the power (as per Eq. 1), is defined as:

$$\bar{a}_n = \frac{1}{N} \sum_{i=1}^N \sum_{k=1}^{K_i} w_{i,k} \frac{\kappa(\vec{\xi}_{i,k})}{\Sigma_t(\vec{\xi}_{i,k})} \psi_n(\vec{\xi}_{i,k}) \rho(\vec{\xi}_{i,k}). \quad (5)$$

In Eq. 5,  $N$  represents the total number of particles in each batch,  $K_i$  is the total number of collisions for particle  $i$ ,  $w_{i,k}$  is the weight of particle  $i$  at collision  $k$ ,  $\kappa(\vec{\xi}_{i,k})$  is the energy released per fission at the phase space point  $\vec{\xi}_{i,k}$ , and  $\Sigma_t(\vec{\xi}_{i,k})$  is the total macroscopic cross section at the phase space point  $\vec{\xi}_{i,k}$ .

While any polynomial basis can be used, a set of orthogonal polynomials is generally preferred. Additionally, by choosing an orthogonal polynomial set whose weighting function  $\rho(\xi)$  equal to unity, Eq. 4 and Eq. 5 can be simplified.

FET implementation often assumes that the solutions are separable. For instance, in cylindrical geometry, the solution is assumed to be separable as:

$$f(r, \theta, z) = g(r, \theta) h(z). \quad (6)$$

This separability offers two key advantages: (1) it significantly reduces memory requirements, especially for large core problems involving Xenon feedback, and (2) it improves particle tracking efficiency by reducing the number of coefficients that need to be tallied. Numerical experiments have demonstrated that separable FET provides a reasonable approximation for non-separable distributions, achieving this at a fraction of the computational cost compared to the fully coupled solution [9].

## 2.2 Polynomials Calculation

As discussed earlier, although any polynomial basis can be used, a set of orthogonal polynomials is generally preferred. In reactor calculations, Legendre and Zernike polynomials are most commonly used. Legendre polynomials serve as the basis for approximating functions in rectangular geometries, while Zernike polynomials are used for cylindrical geometries, such as fuel pellets.

The construction of Legendre polynomials can be done recursively as given by:

$$P_n(x) = \frac{(2n-1)xP_{n-1}(x) - (n-1)P_{n-2}(x)}{n}, \quad (7)$$

with  $P_0 = 1$  and  $P_1 = x$ . Note that when constructing both Legendre and Zernike polynomials, the variable must be scaled into its domain. For example, the Legendre polynomials' variable  $x$  must be scaled over the interval  $[-1, 1]$ . Therefore, if Legendre polynomials need to be calculated across the axial direction of an active reactor core, for instance, from 11.951 cm to 377.711 cm, the variable  $x$  in the range  $[11.951, 377.711]$  must be scaled to the range  $[-1, 1]$ .

Zernike polynomials form an orthogonal set of polynomials defined on a unit disk with variable domain of  $[0, 1]$ . They have traditionally been widely applied in optics, particularly in wavefront analysis due to their ability to represent circularly symmetric functions efficiently [25]. In nuclear reactor simulations, the Zernike polynomial was first adopted to map the power distribution from the SCALE/Denovo radiation transport code to the AMPFuel fuel performance code [26]. Subsequently, it was incorporated into the FET by Ellis [7]. To provide a better illustration on the Zernike polynomials, the first four orders of Zernike polynomials are plotted in Figure 3. Note that, in Figure 3, the Zernike polynomials of order  $Z_n^0$  have a uniform profile across the azimuthal direction.

The radial components of Zernike polynomials are conventionally calculated using the general equation as shown in Eq. 8.

$$R_n^m(r) = \sum_{s=0}^{\frac{n-m}{2}} (-1)^s \frac{(n-s)!}{s! (\frac{n+m}{2}-s)! (\frac{n-m}{2}-s)!} r^{n-2s} \quad (8)$$

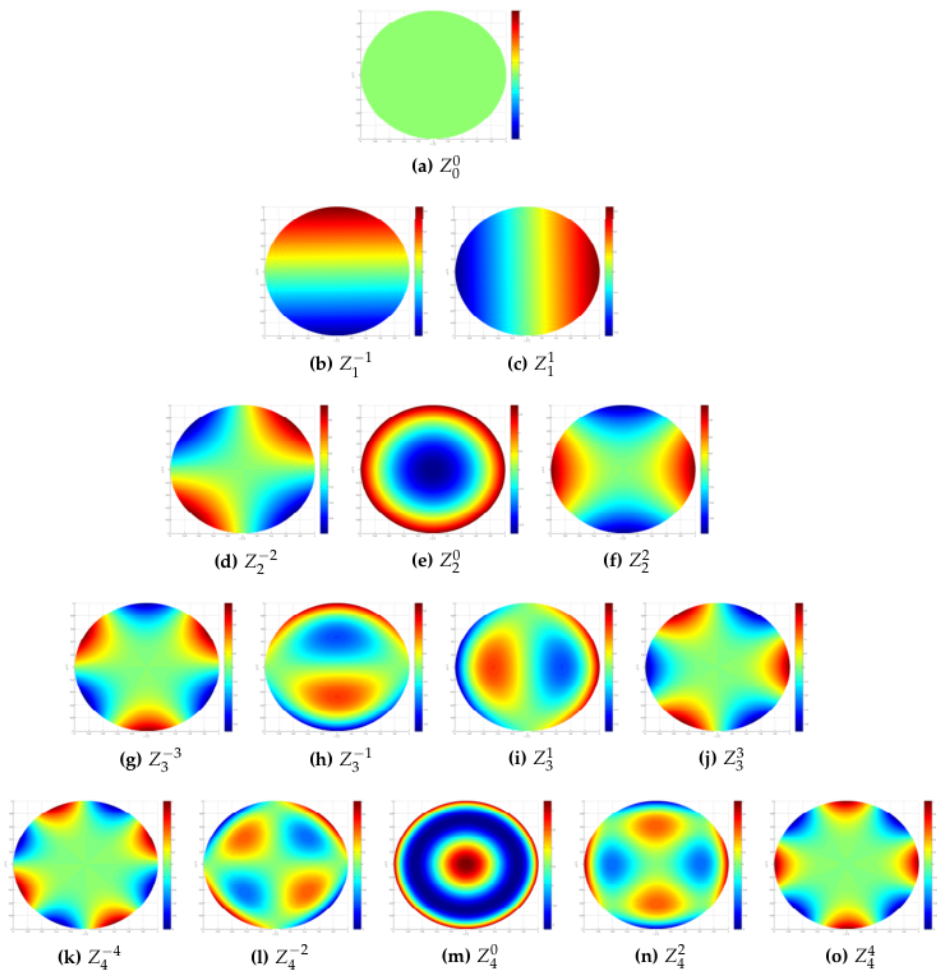


Figure 3. Zernike polynomial orders zero through four. Adapted from [7].

Table 2. CPU time for calculating the radial components of the Zernike polynomials a million times.

Order	CPU time (seconds)		Speedup
	Equation 9	Equation 8	
5	0.0252	0.1179	4.7
10	0.0702	0.6236	8.8
15	0.1450	2.3122	15.9
20	0.2292	8.4591	36.9

In this work, however, we introduce a highly efficient method for constructing the radial components of Zernike polynomials for FET. This approach is based on the recursive technique described in [11], where the radial components are calculated through the following relation:

$$R_n^m(r) = r \left[ R_{n-1}^{|m-1|}(r) + R_{n-1}^{m+1}(r) \right] - R_{n-2}^m(r). \quad (9)$$

In this way,  $R_0^0$ ,  $R_2^0$ ,  $R_3^1$ , and  $R_n^m$  for  $n = m$  can be determined manually as shown in Eq. 10, then followed by the computation of the rest radial components using Eq. 9.

$$\begin{aligned} R_0^0(r) &= 1, \\ R_2^0(r) &= 2r^2 - 1, \\ R_3^1(r) &= 3r^3 - 2r, \\ R_n^m(r) &= r^n \text{ for } n = m. \end{aligned} \quad (10)$$

Table 2 presents a comparison of the CPU time required to calculate the radial components of the Zernike polynomials a million times using Eq. 9 and Eq. 8. As indicated in the table, Eq. 9 provides a more efficient approach for calculating the radial components of Zernike polynomials, particularly at higher orders. This increased efficiency is attributed to its recursive nature, which reduces the number of mathematical operations compared to the conventional method in Eq. 8. This implementation of Zernike polynomial computation represents the first application of this method in FET for reactor core simulations.

Finally, once these radial components are established, the complete Zernike polynomials  $Z_n^m$  can be calculated as follow:

$$Z_n^m(r, \theta) = \begin{cases} R_n^m \cos(m\theta) & \text{if } m > 0, \\ R_n^m \sin(m\theta) & \text{if } m < 0, \\ R_n^m & \text{if } m = 0. \end{cases} \quad (11)$$

However, for MC multi-physics applications in this study, the constructions the radial components for  $m = 0$  only are sufficient under the assumption that power variation within the fuel pellet occurs predominantly along the radial direction, with uniformity along the azimuthal direction.

There exist other orthogonal polynomials that can be used to approximate functions within a unit disk as alternatives to Zernike polynomials. One such example is the Fourier-Bessel series of zeroth

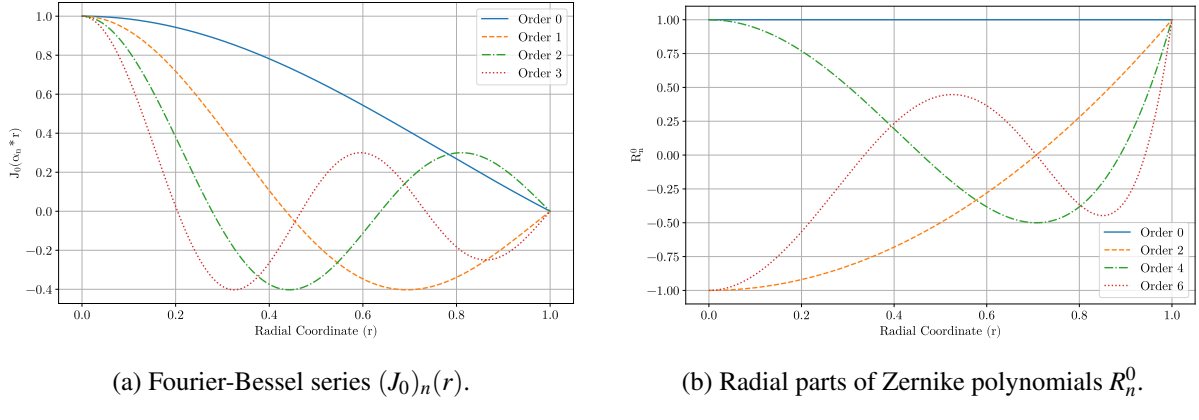


Figure 4. First few orders of Fourier-Bessel series and the radial parts of Zernike polynomials.

order, whose first few modes are shown in Figure 4, alongside the first few radial components of Zernike polynomials. Note that the Fourier-Bessel series of zeroth order are constructed by multiplying the spatial variable with  $\alpha_n$ , which are the positive roots of the zeroth-order Bessel function arranged in ascending order of magnitude, so that

$$(J_0)_n(r) = J_0(\alpha_n r). \quad (12)$$

Where  $(J_0)_n$  denotes Fourier-Bessel series of zeroth order for  $n$ -th order, and  $J_0$  denotes the zeroth order of Bessel function.

However, Zernike polynomials have several advantages over the zeroth-order Fourier-Bessel series:

1. Zernike expansions converge rapidly, meaning that functions can be approximated using fewer terms. For example, to approximate the function  $f(r) = r^2 - 1$ , a Fourier-Bessel expansion requires at least six terms to achieve accurate approximation, while Zernike expansions need only two terms to represent the function exactly, as illustrated in Figure 5.
2. Zernike expansions are generally effective for approximating any functions but may not perform well with rapidly varying functions. In contrast, Fourier-Bessel expansions are only suitable for functions with zero boundary conditions. For instance, Fourier-Bessel expansions approximate the function  $f(r) = r^2$  very poorly, even with 30 terms, as shown in Figure 6. Meanwhile, Zernike expansions can approximate the function accurately.
3. Lastly, Zernike polynomials have a constant weight  $\rho(\vec{\xi}) = 1$ , which simplifies the computation of expansion coefficients, as shown in Eq. 5.

### 2.3 Overcoming Discontinuities

One limitation of the FET method is that its polynomials are primarily effective for approximating smooth distributions, with accuracy decreasing when applied to functions with discontinuities, such as those found in the axial power profile due to the presence of spacer grids. As proposed by Griesheimer

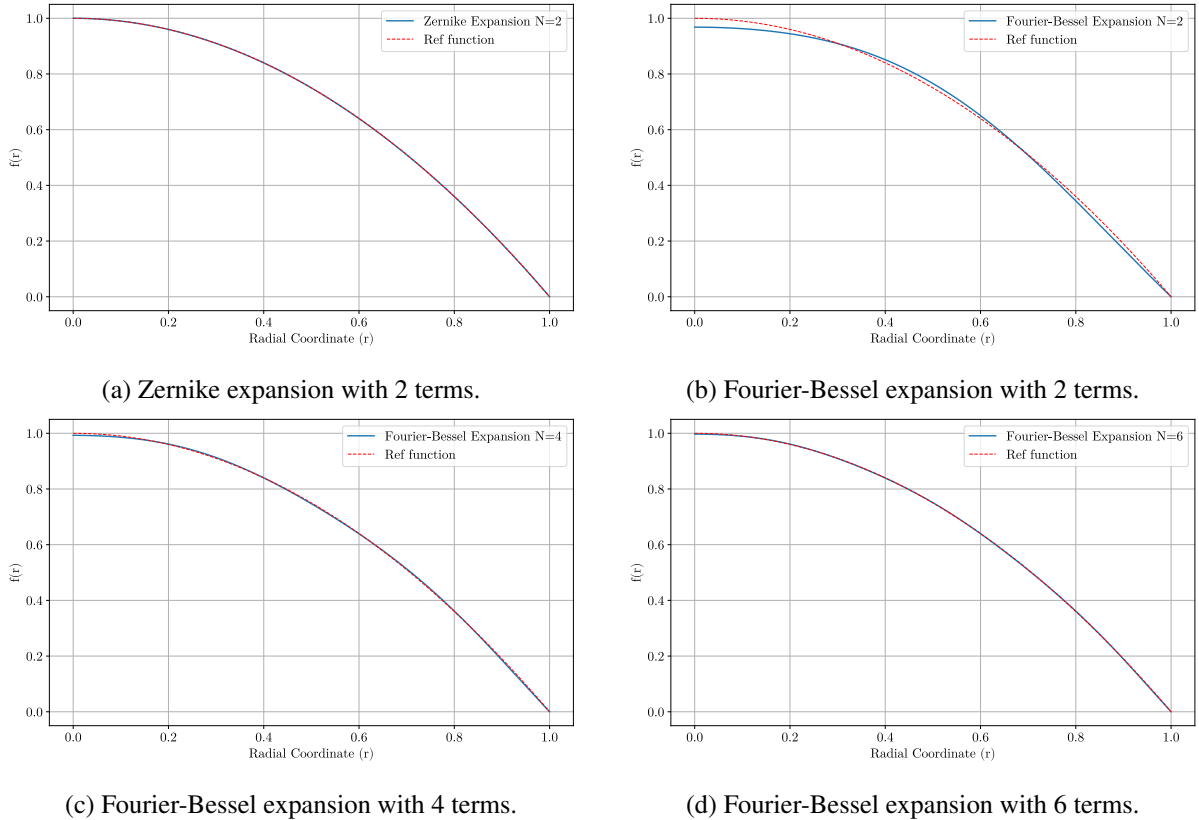


Figure 5. Zernike and Fourier-Bessel expansions to approximate function  $f(r) = r^2 - 1$ .

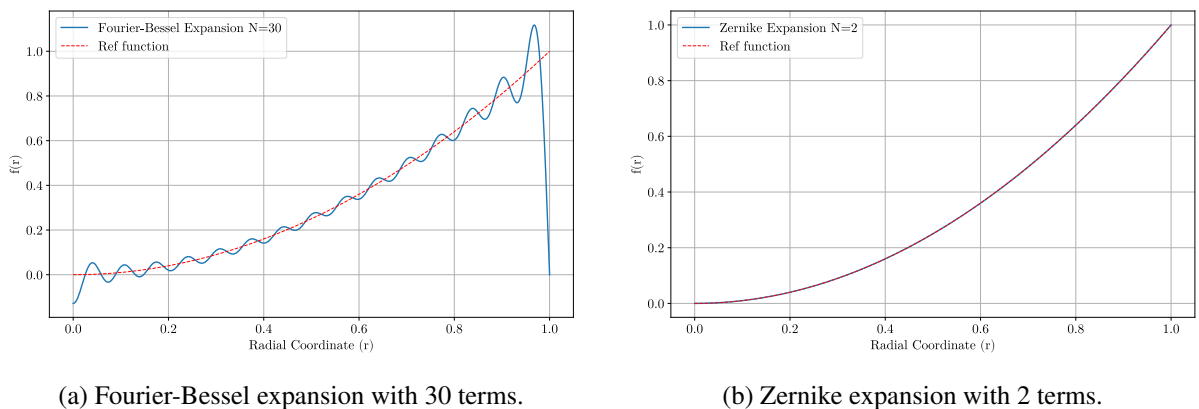


Figure 6. Zernike and Fourier-Bessel expansions to approximate function  $f(r) = r^2$ .

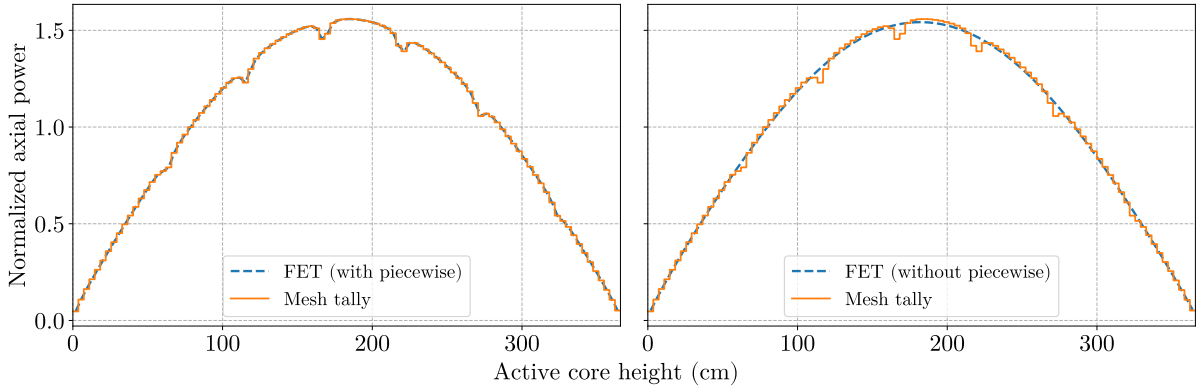


Figure 7. Comparisons of axial power from mesh tally and FET, both with and without the use of piecewise expansions. Both FET cases uses 8<sup>th</sup> order Legendre polynomials expansions.

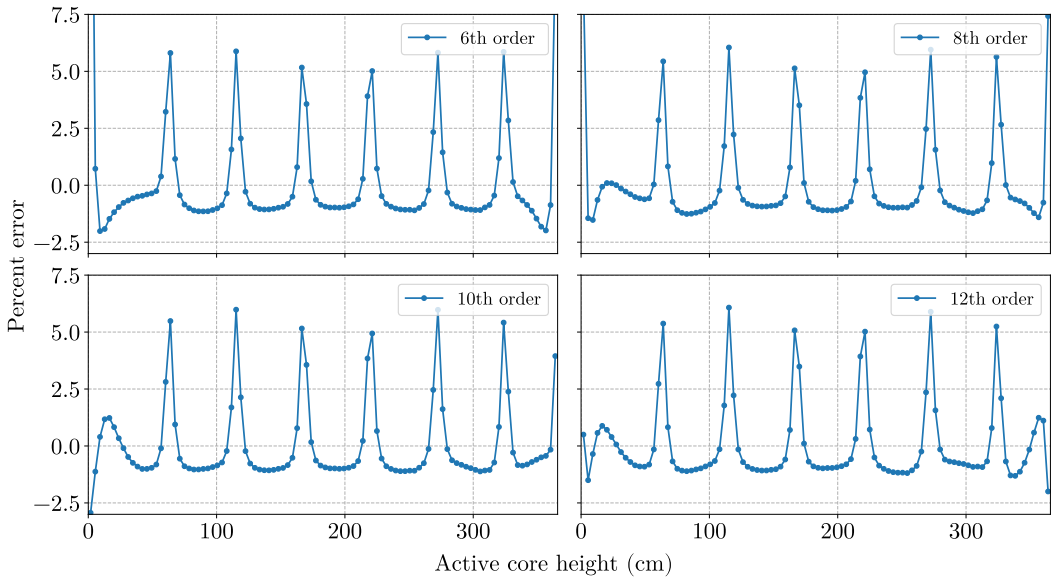


Figure 8. Percent error in axial power from FET without the use of piecewise expansions for 6<sup>th</sup>, 8<sup>th</sup>, 10<sup>th</sup>, and 12<sup>th</sup> order expansions.

[9], this issue can be mitigated by using a piecewise expansion. In this approach, a tally region with known discontinuities is divided into two or more smaller regions, each expected to have a continuous solution, resulting in more accurate approximations.

Figure 7 shows the comparisons of axial power from mesh tally and FET, both with and without the use of piecewise expansions. The FET cases in the figure utilize 8<sup>th</sup> order Legendre polynomial expansions. As demonstrated, the axial power depression due to the presence of spatial grids cannot be accurately modeled using a single expansion, and higher-order Legendre polynomials do not resolve the inaccuracies near power depression areas. As observed in Figure 8, even a 12<sup>th</sup> order expansion does not accurately capture the power depressions in axial power. Conversely, with piecewise expansions, even a 6<sup>th</sup> order expansion can accurately model these depressions as can be seen in the Figure 9.

However, employing piecewise expansions comes with a cost. The use piecewise expansions require

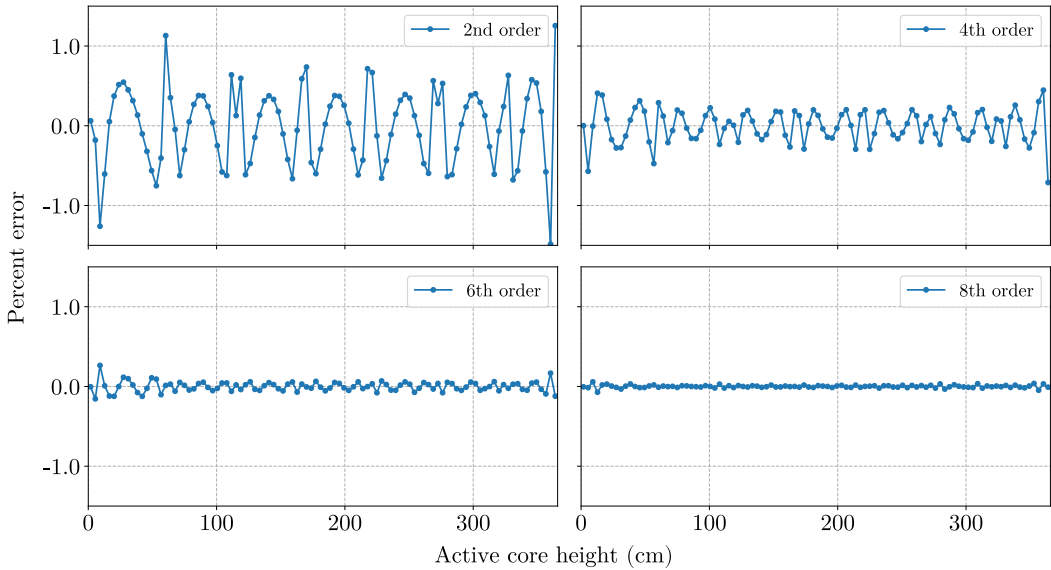


Figure 9. Percent error in axial power from FET with the use of piecewise expansions for 2<sup>nd</sup>, 4<sup>th</sup>, 6<sup>th</sup>, and 8<sup>th</sup> order expansions.

more number expansion coefficients that must be stored because each segmented expansion has its own set expansion coefficients. For instance, in the Watts Bar reactors which have seven spacer grids, the number of 8<sup>th</sup> order Legendre expansion coefficients that must be stored with the use of piecewise expansion is 126 coefficients compared to only 9 coefficients if single expansion is used. Fortunately, as will be shown later, the overall memory savings from utilizing FET are substantial compared to conventional cell tallies in multi-physics simulations.

## 2.4 Variance Estimation

Variance estimation is an integral part in the MC simulations, as lower variance increases confidence in the results. In the implementation of FET in this study, although FET coefficients are tallied during particle tracking, their variances are not directly calculated. Instead, the variances of the reconstructed tallies are computed, as the primary goal of the calculations is not the coefficients themselves but the reconstructed tallies, such as power and reaction rates. The estimated variances for the reconstructed tallies from FET are calculated in a similar manner to traditionally tallied quantities in MC simulations.

## 2.5 Delta-Tracking

Due to the continuous variation of material properties across the fuel pin, delta-tracking is employed as an alternative to conventional surface-tracking. Surface-tracking is not suitable in a continuous medium because the distance to collision is sampled using the following equation:

$$s = -\frac{\ln(\xi)}{\Sigma_t(E)}, \quad (13)$$

which assumes a spatially constant total cross-section  $\Sigma_t(E)$ . If the total cross-section changes during the neutron's random walk, the particle track must be terminated, and a new distance to collision recalculated. Unlike conventional surface-tracking, delta-tracking allows the neutron's random walk to continue through multiple material regions without needing to terminate the particle track at each boundary surface where the change in total cross-section takes place.

Delta-tracking, as described in [27, 28], makes the total interaction probability uniform in all cells, regardless of their material properties, by introducing majorant cross-sections. This allows for the uniform sampling of the distance to collision as given by:

$$s = -\frac{\ln(\xi)}{\Sigma_{maj}(E)}, \quad (14)$$

where  $\xi$  is a uniformly distributed random variable on the interval  $[0, 1]$ , and  $\Sigma_{maj}(E)$  is the majorant cross-section which will be explained later. In this study, to improve rejection sampling efficiency, the interaction probability is made uniform only within the delta-tracking region, which is typically defined at the assembly level.

To preserve the physical nature of neutron transport while allowing the neutron random walk to continue through multiple material regions, the interaction probability in each material is adjusted by introducing virtual collisions. These are rejected collisions based on the total cross section at the neutron's collision site. In practice, this involves rejection sampling, where the collision is only accepted as a physical collision with the probability:

$$p = \frac{\Sigma_t(\vec{r}, E)}{\Sigma_{maj}(E)}. \quad (15)$$

If the probability  $p$  obtained in Eq. 15 is smaller than the newly sampled random number  $\xi$ , the collision is rejected as virtual. In this case, a new distance to collision is sampled using Eq. 14, and the neutron random walk is continued. Conversely, if  $p \geq \xi$ , the collision is accepted as a physical collision, where the actual neutron interaction is simulated and the tally is performed.

Although the value of the majorant cross-section can be chosen arbitrarily, setting it too high can reduce the efficiency of the rejection sampling procedure. Therefore, it is common practice to choose the majorant cross-section as:

$$\Sigma_{maj}(E) = \max[\Sigma_t(\vec{r}, E)]. \quad (16)$$

This ensures that the rejection sampling remains efficient while maintaining the physical nature of the particle tracking.

As previously mentioned, the delta-tracking region is defined within each fuel assembly, resulting in each assembly having a unique majorant cross section. Regions outside the active core still employ the conventional surface-tracking methodology. This approach is used because the geometry outside the active core is relatively straightforward, making the use of delta-tracking less beneficial.

The delta-tracking has a drawback in geometries with significant material heterogeneity, where the total cross sections of different materials vary considerably [29]. A common example is a LWR fuel assembly containing localized heavy absorbers, such as control rods or burnable absorber pins. In these

cases, the absorber's cross section dominates the majorant at low energy, even though it occupies only a small portion of the total volume. This leads to a low probability of sampling a physical collision in regions outside the absorber. The impact of localized high absorbers, as commonly found in LWR problems, on the computational speed will be evaluated in subsection 4.2.

## 2.6 Majorant Cross-Section Computation

One of the main challenges in the delta-tracking for spatially continuous material properties is specifying the majorant cross-section (XS). The continuous distributions of fuel temperature, coolant density, and boron nuclide density significantly influence the XS across the delta-tracking region. Since each nuclide has different energy grids, the majorant XS is stored energy-wise in uniform majorant energy bins (MEB). Each MEB contains one or more energy grids of the point-wise XS in the MC cross-section library.

The calculation of the majorant XS begins by identifying the maximum microscopic total XS within a given MEB for different temperatures. Figure 10 compares the majorant microscopic XS of U-238 across a temperature range of 500 K to 1400 K with the point-wise microscopic XS of U-238 at 700 K. Once the majorant microscopic XSs for each nuclide are determined, they are multiplied by the corresponding highest possible nuclide densities within a given material to obtain the material-wise majorant XS. Finally, the majorant XS for each MEB is determined by selecting the maximum material-wise majorant XS within that MEB, as illustrated in Figure 11.

Numerical experiments suggest that the ideal number of MEBs is 1,200 which distributed across thermal, resonance, and fast regions. If the number of MEBs is too small, rejection sampling becomes inefficient. Conversely, if too many MEBs are used, there is a higher likelihood of underestimating the majorant XS, where it may fall below the actual total XS of the material where the neutron collision occurs. To mitigate this, the maximum total XS is searched for within overlapping MEBs to ensure the largest macroscopic XS is captured for a given energy bin. By optimizing the number of MEBs and using overlapping MEBs, the probability of underestimating the majorant XS can be minimized.

## 2.7 Calculation Flow

The simplified calculation flow of MC coupled multi-physics with spatially continuous material properties is illustrated in Figure 12. The simulation begins with the evaluation of the majorant microscopic cross section, followed by the majorant macroscopic cross section. Particle delta-tracking in a continuous medium proceeds for several cycles, during which FET coefficients are tallied using Eq. 5. After several cycles of particle transport, a thermal-hydraulics (TH) update is conducted. If necessary, updates on critical boron concentration (CBC) and Xenon distribution are also performed.

During the TH update procedure, the two-dimensional nearly continuous power distribution is estimated using the truncated summation of Eq. 1, with coefficients tallied from previous cycles of particle tracking. This power distribution is then utilized by the TH solver to update the temperatures of the fuel, cladding, and coolant, as well as the coolant density. These updated values — two-dimensional

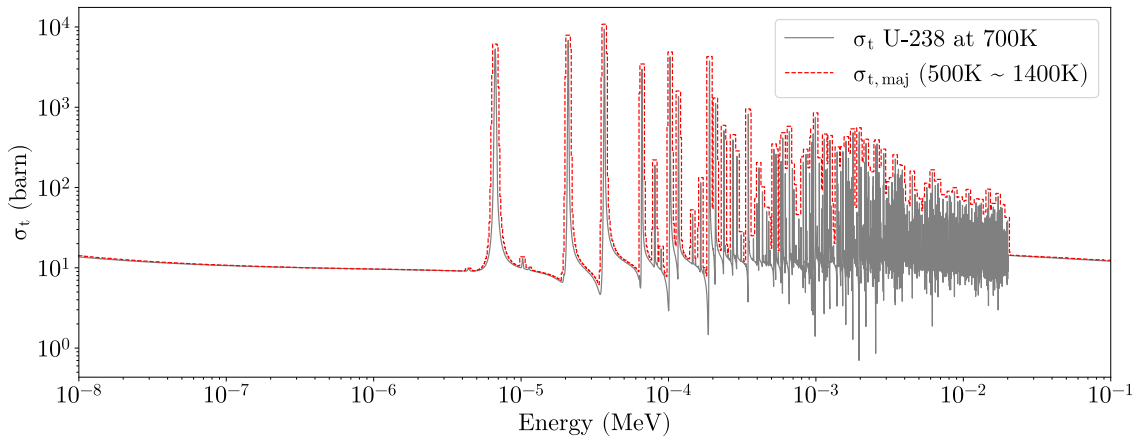


Figure 10. Comparison of majorant microscopic XS of U-238 for temperature ranges 500 K - 1400 K and point-wise energy grid of U-238 at 700 K.

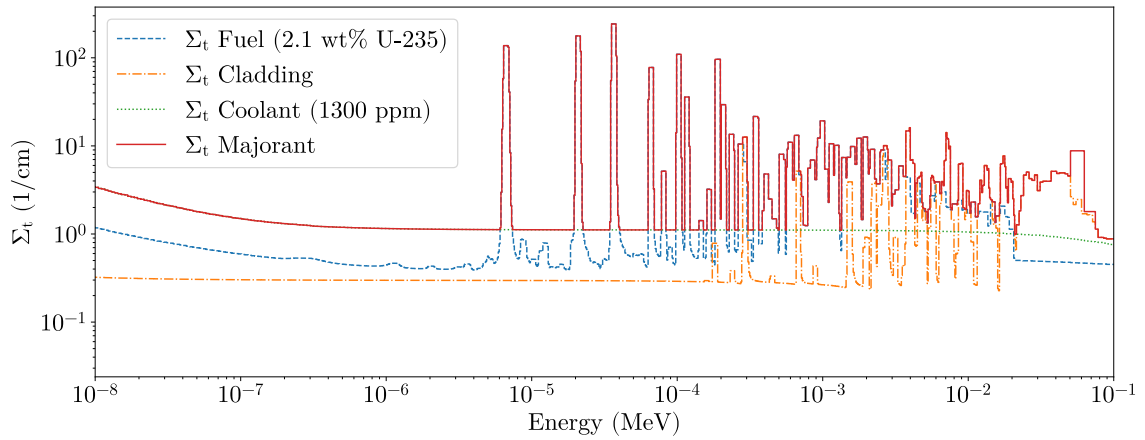


Figure 11. Comparison of majorant macroscopic XS and material-wise majorant macroscopic XS.

fuel temperatures and one-dimensional coolant and cladding temperatures, along with coolant density — are stored for each fuel pin and serve as interpolation points during subsequent particle transport cycles. Similarly, these distributions of material properties are also nearly continuous. If equilibrium xenon feedback is active, a comparable process is used to reconstruct the two-dimensional xenon distribution across the fuel pin. It is worth noting that during inactive cycles, the tallied FET coefficients are discarded at every TH update. However, during active cycles, these FET coefficients are accumulated.

In previous work by Ellis [7, 30], functional expansion was used to represent the continuity of material properties, such as fuel temperature and coolant density. However, using interpolation instead of functional expansion to determine material properties at any point offers a key advantage: it requires fewer arithmetic operations than polynomial reconstruction, thus enhancing particle tracking efficiency.

The calculation of macroscopic cross sections for particle tracking in spatially continuous materials differs from conventional methods, where each cell is assigned unique material properties. In the case of particle tracking within spatially continuous materials, when a neutron is in the fuel pellet, a two-dimensional interpolation in both the axial and radial directions is employed to determine the fuel temperature at given spatial point. When a neutron in the coolant, a one-dimensional interpolation in the axial direction determines the temperature and density at given spatial point, followed by updates to the nuclide densities in the coolant. Lastly, for a neutron in the cladding, a one-dimensional interpolation in the axial direction determines the cladding temperature. After these temperatures and densities are determined, the microscopic cross section for a given energy and temperature is calculated for all nuclides within the material. Finally, the macroscopic cross section at the neutron's location is computed. These processes are summarized in Figure 13.

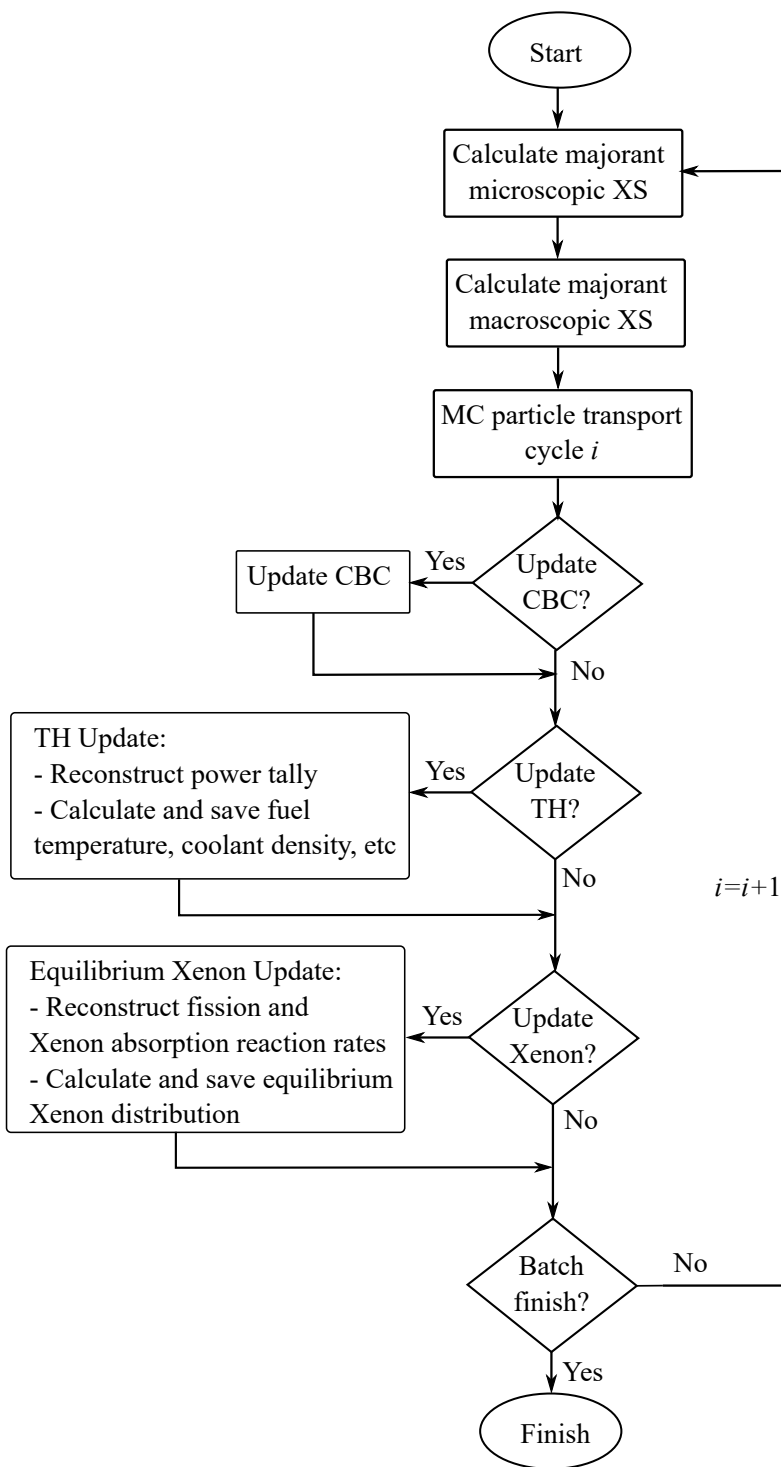


Figure 12. Calculation flow of the proposed framework.

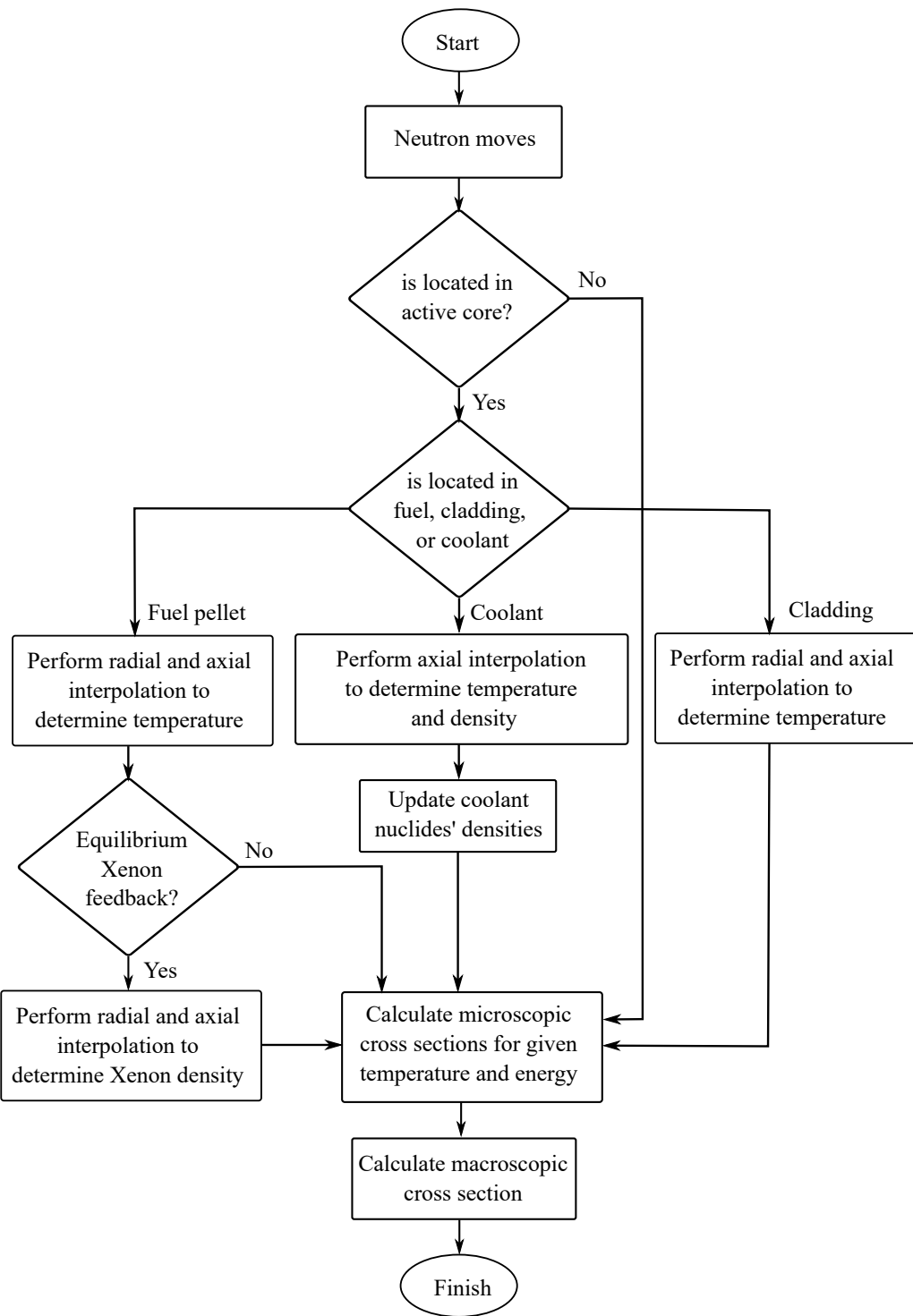


Figure 13. Calculation flow to calculate macroscopic cross section in spatially continuous particle transport.

### III Thermal Expansion

This section explains the theory behind thermal expansion (TE), with a particular focus on the on-the-fly thermal expansion implementation in the MCS code. Subsection 3.1 provides a brief overview of the fundamental theory of thermal expansion, followed by a discussion on the specific thermal expansion coefficients utilized in this study in subsection 3.2. Subsection 3.3 describes multi-physics coupling in the MCS code. The detailed implementation of on-the-fly thermal expansion is thoroughly explained in subsection 3.4. Finally, the calculation flow for the on-the-fly thermal expansion methodology is described in subsection 3.5.

#### 3.1 Theory

The theory of thermal expansion is relatively straightforward, and it will be described here. The physical model for the linear thermal expansion of solid materials with an isotropic crystal structure is given by:

$$L = L_0 [1 + \alpha_L (T - T_{ref})], \quad (17)$$

here  $L$  is the final length at temperature  $T$ ,  $L_0$  is the original length at reference temperature  $T_{ref}$ , and  $\alpha_L$  is the coefficient of linear thermal expansion. This formula applies to solid materials where the thermal expansion is assumed to occur uniformly in all directions. In nuclear reactors, thermal expansion affects various core components, such as fuel rods, cladding, and structural elements, due to temperature changes during operation.

Similarly, the physical modelling for area thermal expansion, such as fuel pellet area, is given by:

$$A = A_0 [1 + \alpha_L (T - T_{ref})]^2, \quad (18)$$

where  $A$  and  $A_0$  are the final and initial area respectively. This area thermal expansion is used to calculate radial expansion for the fuel pellet,

When materials undergo thermal expansion, it is essential to preserve the mass, which requires adjusting the material densities to reflect the expanded dimensions. The density modification can be expressed as:

$$\rho = \rho_0 \frac{V_0}{V}, \quad (19)$$

where  $\rho$  and  $V$  represent the thermally expanded density and volume, respectively, while  $\rho_0$  and  $V_0$  denote the initial density and volume, respectively. The thermally expanded volume can be calculated using the expanded length  $L$  and area  $A$ , shown in Eq. 17 and Eq. 18, respectively.

#### 3.2 Thermal Expansion Coefficients

The thermal expansion coefficients of materials used in reactors are crucial for accurate thermal expansion modeling. Detailed descriptions of the correlations used to determine these coefficients for typical materials in light water reactors (LWRs) are provided in reference [12]. However, this work

Table 3. Thermal expansion coefficients used in this study.

Material	Thermal expansion coefficients ( $K^{-1}$ )
Zirconium alloys (fuel cladding)	$7.00 \times 10^{-6}$
SS304 (core plate)	$1.78 \times 10^{-5}$
UO <sub>2</sub> (Fuel pellet)	$1.10 \times 10^{-5}$

adopts the thermal expansion coefficients used in the STREAM code [31]. These coefficients are summarized in Table 3.

Note that these thermal expansion coefficients are similar to those described in Palmtag et al. [12]. Additionally, this study limits thermal expansion modeling to the fuel pellet, cladding, pin pitch, and assembly pitch. The dimensions of absorber materials, such as control rods and burnable absorbers, are assumed to remain constant.

### 3.3 Thermal-Hydraulics Coupling

MCS is a neutron/photon transport code that can be coupled with both TH1D [32] and CTF [33]. TH1D is a simple closed channel TH solver initially developed for nTracer TH solver. It solves mass and energy conservation equations in one-dimensional axial direction and does not consider phase change. While CTF is a more sophisticated TH solver that solves all the three conservation equations including the momentum equation, both for fluid and vapor phases, and in three dimensional directions. Also, CTF has a capability to model spacer grids, but the effects of spacer grids on the TH calculations were omitted in this study.

Both TH1D and CTF are internally coupled with MCS, allowing data transfers between MCS and the TH solvers to occur automatically. Although the solvers must be compiled separately, they are linked through a static library. Linear power from MCS is transferred to the TH solvers, while TH parameters are updated by TH solvers and returned to MCS. These data transfers are performed at the pin-by-pin level.

Since data transfers are performed at the pin-by-pin level, MCS multi-physics coupling always uses a single pin cell as the channel for TH coupling. For example, in a single fuel assembly with a  $17 \times 17$  configuration, including 24 guide tubes and one instrumentation tube, a total of 264 channels are modeled for TH coupling. The reactor's TH parameters are updated regularly after several cycles of MCS particle tracking. During MCS particle tracking, fission power is tallied in both inactive and active cycles. In inactive cycles, the power tally is not accumulated, meaning that the tally from the last TH update is discarded. In contrast, during active cycles, when both the fission source and TH parameters have converged, the fission power tally is accumulated.

The fission power is tallied for each cell in the fuel pellets and then converted into linear powers. These linear powers are passed to the TH solvers to update the reactor's TH parameters, such as fuel, cladding, and coolant temperatures, as well as coolant densities. These TH parameters are then used to update the nuclide cross sections in the MCS code for subsequent cycles of neutron transport until

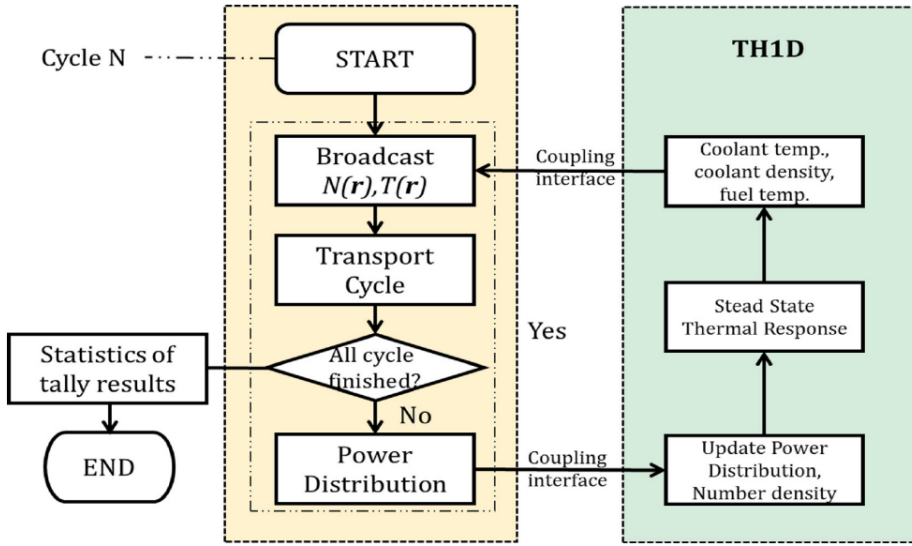


Figure 14. Flow chart of MCS-TH1D coupling interface. Adapted from [34].

the next TH update. These procedures are repeated until all cycles are completed. The detailed flow chart of these iterative methods is shown in Figures 14 and 15 for MCS-TH1D and MCS-CTF coupling, respectively.

### 3.4 On-The-Fly Thermal Expansion

Many MC codes, such as MCS, use Constructive Solid Geometry (CSG) to define the geometry of reactor problems. Performing non-uniform geometrical expansion using local temperatures in CSG presents a challenge because a single surface can be reused to form multiple cells within a universe, and a universe can be repeatedly used to define a lattice. Consequently, modifications to a particular surface, such as those resulting from thermal expansion, can affect all cells, universes, and lattices that utilize the modified surface. One possible solution to avoid this issue is by creating copies of surfaces and cells, so that every cell can be expanded according to their respective local temperatures. However, this approach is cumbersome for large reactor problems and would consume more memory.

To address this problem, on-the-fly thermal expansion is introduced. In this approach, when a particle enters a particular pin, the geometry of fuel pellet and cladding in that fuel pin are expanded using the corresponding local temperatures, which can be either pin-averaged or assembly-averaged temperatures. Similarly, the pin and assembly pitches where the particle is located are also expanded according to the assembly-averaged and core-averaged temperatures, respectively. In both the pin-averaged and assembly-averaged temperature cases, the average temperatures are calculated in both the axial and radial directions using volume-weighted averaging.

In the implementation in MCS, the fuel pellet expanded both in radial and axial directions, while the cladding is expanded only in the radial direction, with the inner and outer radius assumed to expand equally. It should be noted that geometry deformation is assumed to be uniform both radially and axially, which implies that, for instance, fuel cladding ballooning is not considered. These expansions

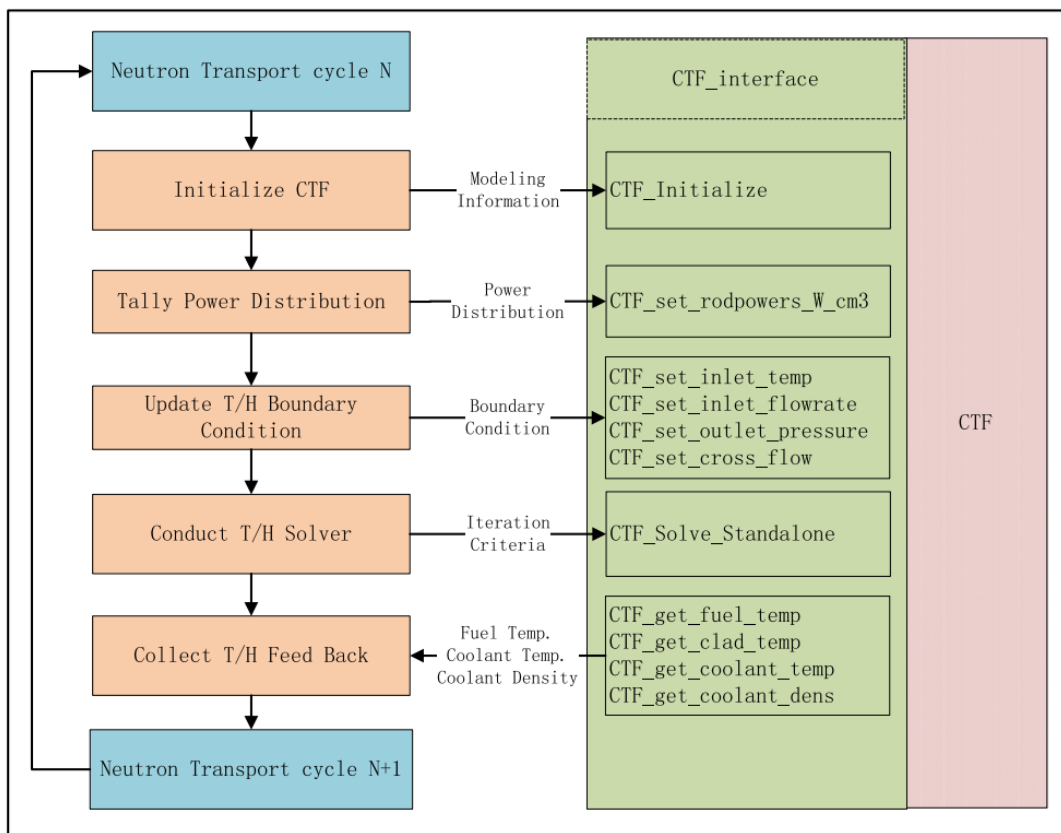


Figure 15. Flow chart of MCS-CTF coupling interface. Adapted from [34].

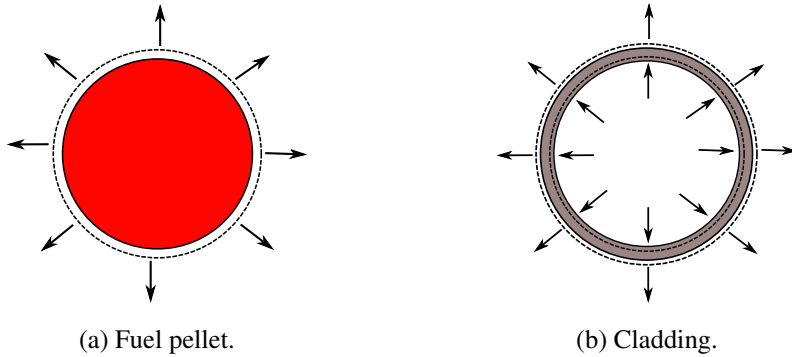


Figure 16. The radial expansion of fuel pellet and cladding.

are illustrated in Figure 16.

### 3.5 Calculation Flow

Figure 17 is a flow chart illustrating the calculation of geometrical changes due to thermal expansion. Initially, after several cycles of neutron tracking, the thermal-hydraulic (TH) solver is executed to determine the temperature distribution. This temperature distribution is then used to calculate pin-averaged fuel pellet and cladding temperatures, which are subsequently utilized to determine the corresponding expansion-induced geometrical changes in fuel pellets and cladding. Similarly, assembly-averaged temperatures are used to compute the geometrical changes in pin-pitch. Following this, core-averaged temperatures are used to thermally expand the assembly pitches uniformly. Finally, the material densities are updated to ensure the preservation of material mass throughout the process. These steps are repeated iteratively until all cycles are completed.

Once the geometrical changes due to thermal expansion are calculated during the TH update, this information is used to thermally expand the core geometry on-the-fly during subsequent cycles of neutron tracking. When a neutron is located in a pin cell after performing a random walk, MCS checks whether it originated from another pin cell or from the same one. If it originated from another pin cell, the fuel pellet and cladding surfaces in that pin cell are expanded based on the previously calculated geometrical changes. Additionally, if the neutron came from another assembly, the pin pitches within that assembly are uniformly expanded as well. These steps are summarized in Figure 18.

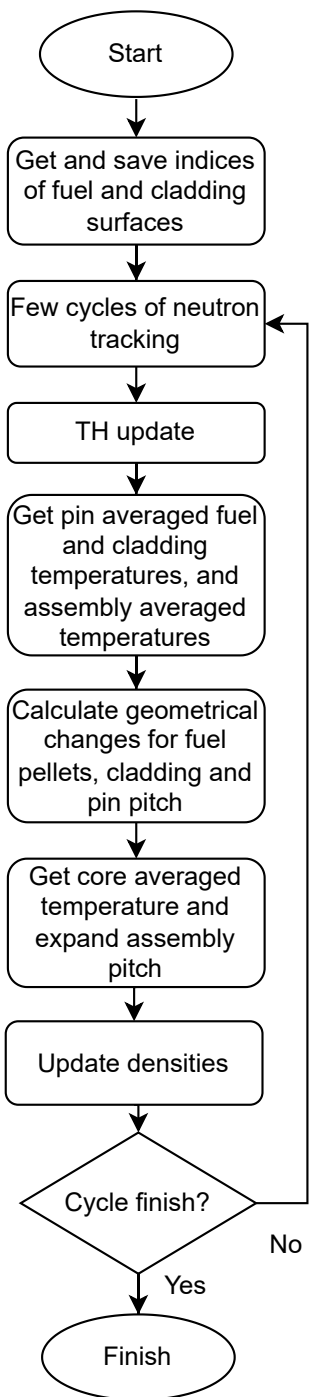


Figure 17. Calculation of geometrical changes due to thermal expansion.

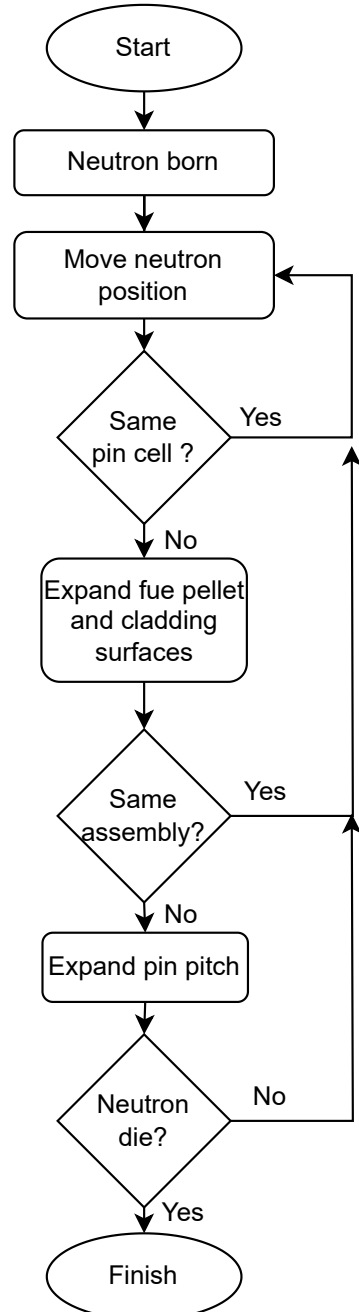


Figure 18. On-the-fly thermal expansion during neutron tracking.

## IV Numerical Results

With the theoretical background described in the previous sections, this section demonstrates the capabilities of the proposed framework in addressing multi-physics problems using several test cases, ranging from two-dimensional pin-cell problems to whole-core problems. Most of the problems presented in this thesis use material compositions and geometry from the Virtual Environment for Reactor Applications (VERA) core physics benchmark [35]. Additionally, ENDF/B-VII.1 was used for the MCS cross section library.

This section is divided into three major subsections. Subsection 4.1 briefly describes the VERA reactor benchmark used for the numerical test problems in this thesis. Subsection 4.2 provides the solutions for MC coupled multi-physics with spatially continuous material properties. While the solutions for thermal expansion are presented in subsection 4.3. Lastly, subsection 4.4 presents the solutions for assembly and whole-core problems using both spatially continuous material and thermal expansion methods.

### 4.1 Benchmark Description

The reactor operational data for the VERA benchmark were taken from Watts Bar Generating Station Unit 1, operated by the Tennessee Valley Authority (TVA) since 1996. This reactor is a 3411 MWth Westinghouse pressurized water reactor (PWR) with 193 fuel assemblies and an active core height of 365.76 cm. Each fuel assembly contains a  $17 \times 17$  array of pins, consisting of 264 fuel pins, 24 guide tubes, and 1 instrumentation tube as shown in Figure 19. Eight spacer grids are used for each assembly to maintain its structural integrity. Radially, the fuel-assembly pitch is 21.5 cm, with fuel pins within an assembly having pitch of 1.26 cm. In a  $17 \times 17$  array of pins, this results in a 0.04 cm inter-assembly gap. These inter-assembly gaps are essential to accommodate fuel assembly deformation due to thermal expansion. The fuel pin consists of a fuel pellet with a radius of 0.4096 cm, along with a gap and cladding, as illustrated in Figure 20.

During the first cycle, the reactor employed three different fuel enrichments: 2.11%, 2.62%, and 3.10% by weight of U-235, and Pyrex burnable absorbers were used. Reactor regulation is provided by 57 control rod assemblies, grouped into 8 banks, as illustrated in Figure 21. Pyrex is a discrete burnable neutron absorber typically used in Westinghouse reactors, made from borosilicate glass ( $\text{B}_2\text{O}_3\text{-SiO}_2$ ), and inserted into assembly guide tubes. These inserts can be placed in any assembly not located in a control rod position. The control rod is an axial stack of Silver-Indium-Cadmium (AIC) and boron carbide ( $\text{B}_4\text{C}$ ). A set of 24 control rods are clustered into a reactor cluster rod assemblies (RCCAs) to control and ensure a safe core shut down. The tips of the control rods are made from AIC and the remaining portions up to the plenum are made from  $\text{B}_4\text{C}$ .

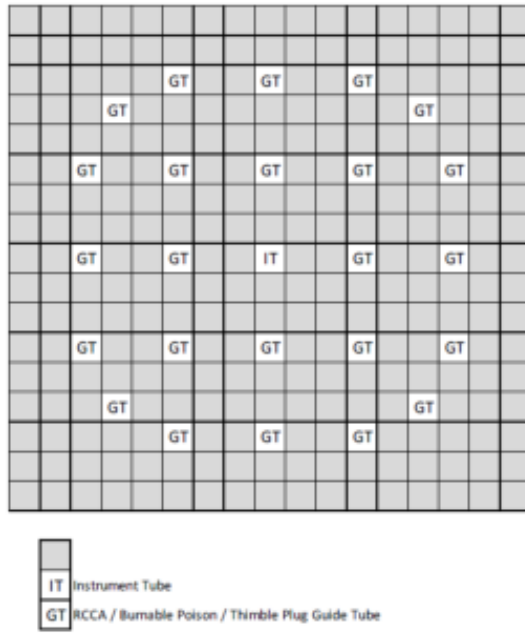


Figure 19. Fuel assembly radial layout. Adapted from [36].

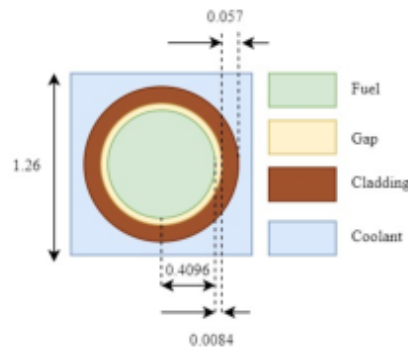


Figure 20. Fuel rod radial layout. Adapted from [36].

	H	G	F	E	D	C	B	A
8	2.1 20	2.6 20	2.1 20	2.6 20	2.1 20	2.6 20	2.1 12	
9	2.6 20	2.1 24	2.6 24	2.1 20	2.6 20	2.1 24	3.1 24	3.1 31
10	2.1 24	2.6 24	2.1 20	2.6 20	2.1 20	2.6 16	2.1 8	
11	2.6 20	2.1 20	2.6 20	2.1 20	2.6 20	2.1 16	3.1 31	
12	2.1 20	2.6 20	2.1 20	2.6 20	2.6 24	2.6 24	3.1 31	
13	2.6 20	2.1 16	2.6 16	2.1 24	2.6 24	3.1 12	3.1 31	
14	2.1 24	3.1 24	2.1 20	3.1 16	3.1 16	3.1 12		
15	3.1 12	3.1 8	3.1 8	3.1 12				
					Enrichment Number of Pyrex Rods			

	H	G	F	E	D	C	B	A
8	D		A		D		C	
9						SB		
10	A		C				B	
11				A		SC		
12	D				D		SA	
13		SB		SD				
14	C		B		SA			
15								

Figure 21. VERA benchmark core configuration and control rods layout. Adapted from [35].

Table 4. Two-dimensional pin-cell problem infinite multiplication factors.

Cases	# radial discretization	$k_{inf}$
A1	1	$1.22203 \pm 0.00002$
A2	5	$1.22250 \pm 0.00002$
A3	20	$1.22259 \pm 0.00002$
FET	N/A	$1.22261 \pm 0.00002$
Extrapolation	N/A	1.22262

## 4.2 Spatially Continuous Material Properties

This subsection presents and discusses the solutions for MC coupled multi-physics simulations with spatially continuous material properties. For multi-physics feedback in all problem cases in this subsection, unless specified otherwise, radial heat conduction calculations within the fuel pellet were conducted using 10 radial rings, while a single mesh was employed for the gap and cladding regions. The resulting radial fuel temperature distribution was then averaged based on the number of radial cells used in the neutronic calculations.

In the conventional or cell-based approach, the problem geometry was discretized into several cells, with material properties such as temperature and density being uniform within each cell. This discretization was necessary to capture material property variations across the problem geometry. In contrast, in the FET-based cases, explicit problem geometry discretization was unnecessary. Instead, the power and Xenon absorption rates distributions were reconstructed using 100 axial and 10 radial equidistant meshes for each pin during each TH update and equilibrium Xenon feedback, respectively.

For tally reconstruction, seventh-order Legendre polynomials and ninth-order Zernike polynomials were used in the axial and radial directions, respectively.

### 4.2.1 Two-dimensional Pin-cell Problem

This two-dimensional pin-cell problem, based on the work of Choi and Joo [5], is designed to evaluate the temperature distribution within a fuel pellet and its influence on spatial self-shielding. The case involves a two-dimensional pin-cell multi-physics model, utilizing UO<sub>2</sub> fuel enriched to 2.1 wt.% and a linear power density of 175 W/cm. To maintain a constant axial profile, the coolant flow rate is assumed to be infinite. The coolant bulk temperature is fixed at 600K, with no boron dilution in the coolant.

Three cases are presented in this problem, as outlined in Table 4. Each case varies in the number of radial cells used for neutronic calculations. Cases A1, A2, and A3 are cell-based, with discretization into 1, 5, and 20 equally spaced radial cells, respectively. The results from these cases are compared to those obtained from the FET case, which utilizes continuous fuel temperature. It is important to note that all simulations used  $5 \times 10^4$  particles per cycle, over a total of 30,000 cycles, with 27,500 cycles designated as active.

The continuous fuel temperature from the FET case is compared to the piecewise fuel temperature

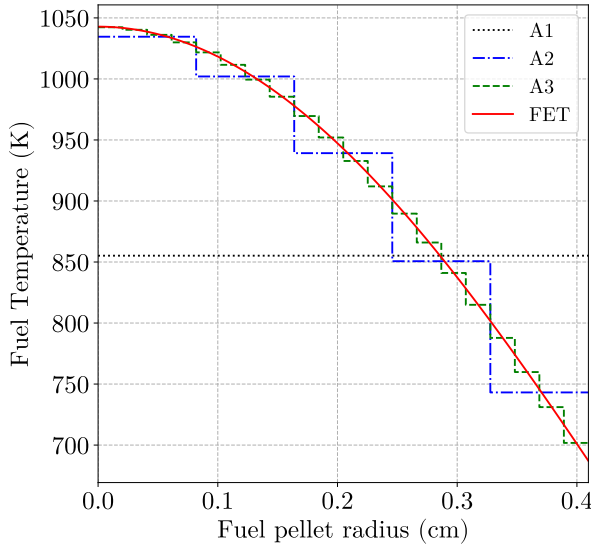


Figure 22. Radial fuel temperature distribution for two-dimensional pin-cell problem.

from the other cases in Figure 22. As shown, the continuous temperature from the FET case closely aligns with the piecewise fuel temperature as the mesh refinement increases. For a direct comparison, radial mesh tallies for absorption and fission rates across 20 meshes were conducted during the simulation, with the results displayed in Figure 23. The figure demonstrates that the proposed framework yields increasingly accurate solutions as the mesh size decreases, which confirms the correct implementation of the framework into the MCS code. The differences in absorption rates between cases A2 and A3 and the FET case are less than 1.0%, while the A1 case overestimates the self-shielding absorption at the fuel pellet's periphery by up to 2.6%, due to the higher peripheral fuel temperature in the A1 case. In contrast, the fission rate remains relatively uniform with no significant differences, as thermal neutrons that responsible for fission are less affected by self-shielding. The combination of higher resonance absorption at the fuel pellet periphery and a relatively flat fission rate distribution results in a lower infinite multiplication factor ( $k_{inf}$ ), as observed in the A1 case (see Table 4).

To verify that the  $k_{inf}$  from the FET case asymptotically approaches the solution obtained with infinitesimal cell sizes, a quadratic extrapolation was conducted. This extrapolation uses Lagrange basis polynomials, with the variable defined as the inverse of the number of radial rings. The extrapolated  $k_{inf}$  is shown in Table 4, and the extrapolation result is plotted in Figure 24. As illustrated, the extrapolated  $k_{inf}$  lies within the uncertainty range of the  $k_{inf}$  value obtained from the FET case.

These results demonstrate that the FET solutions asymptotically converge to those obtained from conventional cell-based discretized simulations with infinitesimally small cells. Furthermore, modeling radial temperature variations in the fuel pellet is essential for obtaining more accurate reactivity effects.

#### 4.2.2 Three-dimensional Pin-cell Problem

This three-dimensional pin-cell problem employs UO<sub>2</sub> fuel with 2.1 wt.% enrichment and involves two Inconel spacer grids at the top and bottom, with five Zircaloy spacer grids positioned in between.

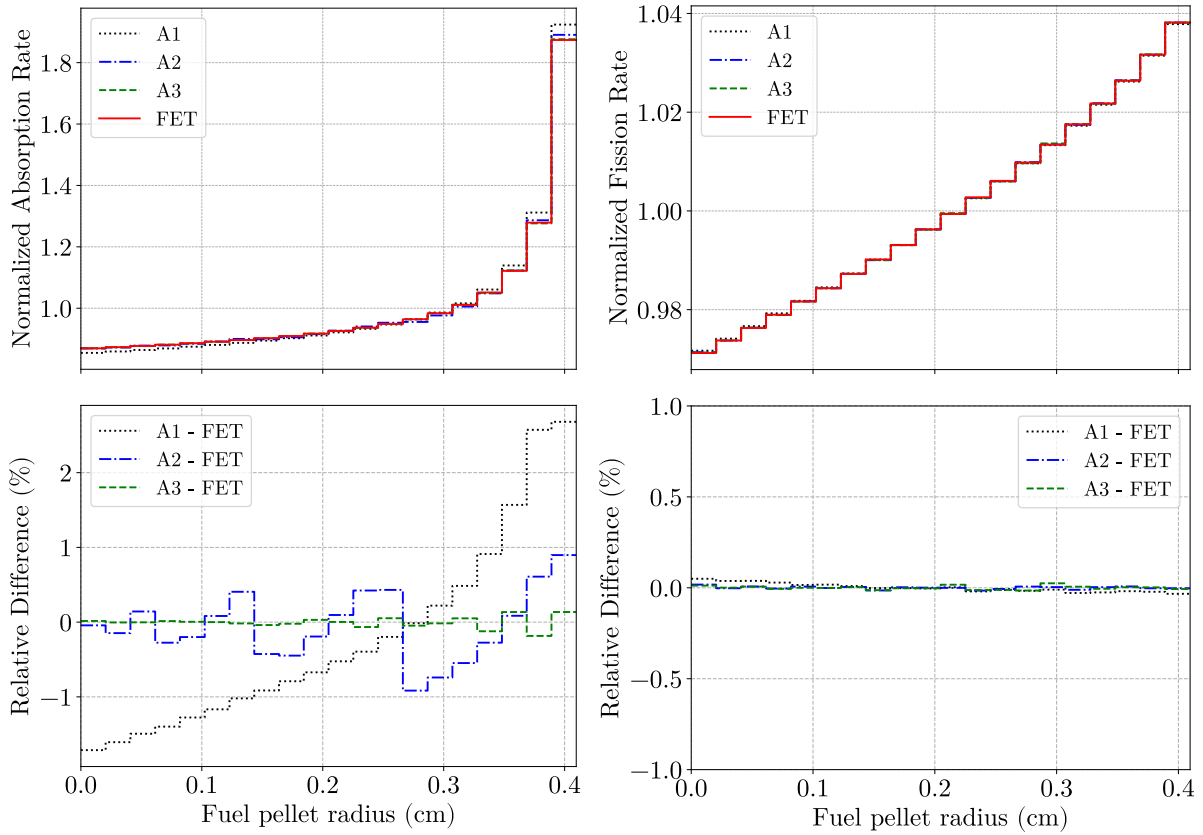


Figure 23. Normalized absorption and fission rates, and their respective relative differences for the two-dimensional pin-cell problem.

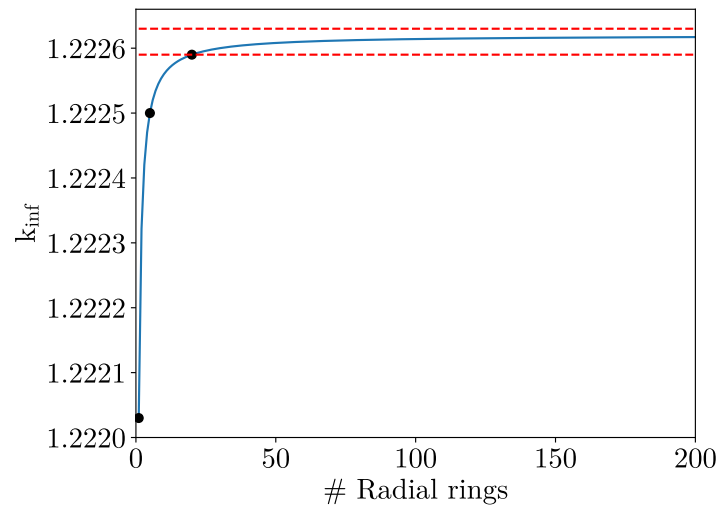


Figure 24. Extrapolated  $k_{inf}$  for two-dimensional pin cell problem.

Table 5. Calculation results for three-dimensional pin-cell problem.

Cases	# of fuel pellet axial/radial discretization	Critical Boron Concentration (ppm)	Relative wall-clock time
B1	25/1	$1507.5 \pm 0.3$	1.2
B2	100/5	$1511.1 \pm 0.3$	4.5
FET	N/A	$1512.5 \pm 0.3$	1.0

This test problem is a critical boron concentration (CBC) search problem at full power, corresponding to 67 kW of thermal power. Unlike previous problem, this problem includes equilibrium Xenon feedback.

Three cases were developed for comparison with the proposed framework. The first two cases, B1 and B2, are cell-based, where the problem domain is discretized into several cells. In the B1 case, the domain is divided into 25 axial cells and 1 radial cell, while in the B2 case, it is discretized into 100 axial cells and 5 radial cells (for the fuel pellet). The finer mesh in the B2 case is essential for capturing smoother distributions of fuel temperature, Xenon number densities (both radially and axially), and coolant density (including boron nuclide concentrations) along the axial direction. All cases simulated  $5.0 \times 10^4$  particles per cycle over 22,500 cycles, with 20,000 active cycles.

Table 5 compares the CBC results from all cases, showing that the solutions converge toward those obtained from the FET case as the cells' sizes become infinitesimal. This convergence is mainly due to a more accurate representation of the radial intra-fuel-pellet temperature distribution, leading to improved modeling of the self-shielding effect.

Figure 25 illustrates the radially-averaged power, fuel temperature, and coolant density, which exhibit good agreement between cases. To further verify the accuracy of the FET case, a 100-bin axial mesh tally was performed in all cases, and percentage differences, along with one-sigma standard deviations, are presented in Figure 26. As shown, the axial power differences and corresponding standard deviations between the FET and B2 cases are less than 0.5%. These comparisons demonstrate the higher accuracy achievable with the proposed approach.

In addition, Table 5 demonstrates that, despite its greater accuracy, the FET case has the shortest run-time. It is 1.2 and 4.5 times faster than the B1 and B2 cases, respectively. This performance improvement primarily due to reduced number of cells, which optimizes delta-tracking in two key ways. First, with fewer particle crossings, material-wise macroscopic cross-sections are computed less frequently. Second, with fewer cells, the recursive routine for determining particle location is more efficient. Moreover, in cases without localized neutron absorbers, such as burnable poisons or control rods, the rejection sampling for delta-tracking in the FET case can be performed more efficiently.

#### 4.2.3 Three-dimensional Assembly Problem

This three-dimensional assembly problem is identical to Problem #6 from the VERA benchmark [35], using 3.1 wt.% enriched fuel pellets. This problem is simulated at hot full power (HFP), equivalent to 17.67 MW of thermal power, with 1300 ppm of boric acid diluted in the coolant. Unlike previous

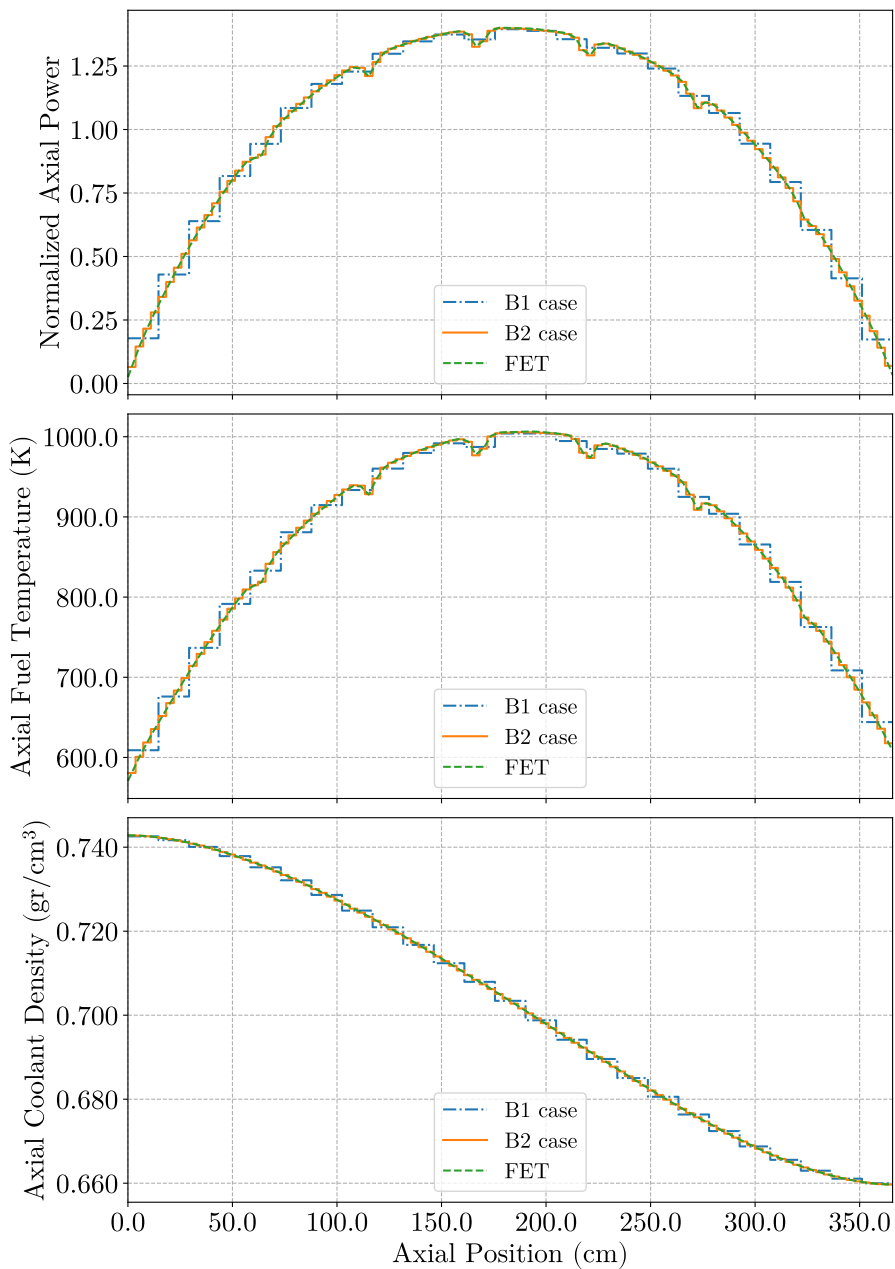


Figure 25. Normalized axial power, fuel temperature, and coolant density for B2 and FET cases.

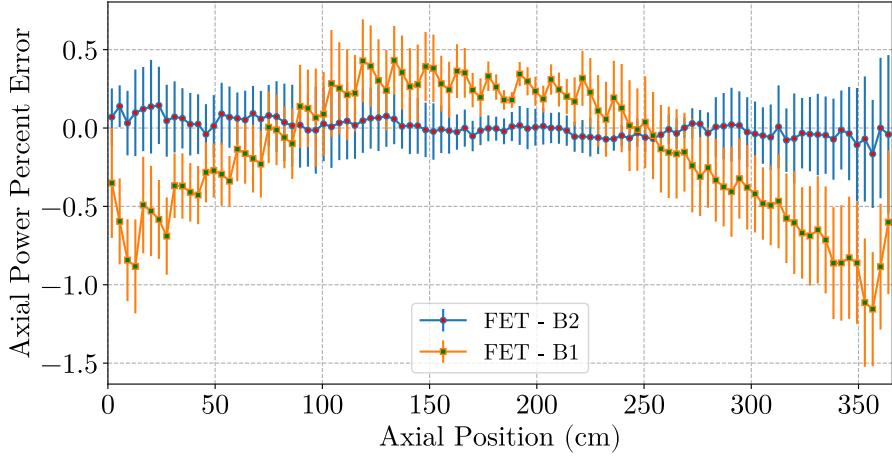


Figure 26. Axial power percentage differences of the FET case against B1 and B2 cases, and their corresponding one sigma of standard deviations.

Table 6. Calculation results for three-dimensional assembly problem.

Cases	# of fuel pellet axial/radial discretization	$k_{inf}$	Relative wall-clock time
C1	25/1	$1.16400 \pm 0.00004$	1.6
C1	50/2	$1.16443 \pm 0.00004$	2.3
C2	100/5	$1.16449 \pm 0.00005$	5.1
FET	N/A	$1.16465 \pm 0.00004$	1.0 <sup>(a)</sup>

<sup>(a)</sup> The absolute wall-clock time for the FET case is 1.8 hours with 70 MPI processes.

problem cases, this problem includes non-fuel structural materials such as the pin plenum, nozzles, core plates, and axial reflectors. Figure 27 illustrates the three-dimensional assembly problem.

Four cases were developed for comparison with the proposed framework. The first three cases, C1, C2, and C3, are traditional cell-based models where the problem domain is discretized into multiple cells. In case C1, the problem is divided into 25 equidistant axial cells without radial discretization. Case C2 refines this by using 50 equidistant axial cells and 2 equivolume radial rings in the fuel pellet to capture the temperature distribution within the pellet both radially and axially. Case C3 further increases the refinement to 100 equidistant axial cells and 5 equivolume radial rings. While FET case employs spatially continuous material properties.

Each case simulated  $3 \times 10^4$  particle histories per cycle, with a total of 12,500 cycles, of which 2,500 were designated as active cycles. The eigenvalue comparisons are shown in Table 6. As with the previous test problems, as the cell sizes become infinitesimal, the eigenvalue increases and asymptotically approaches the value from the FET case. The FET eigenvalue was also independently compared against the MC21/CTF solution [2], with the MC21/CTF eigenvalue being approximately 40 pcm lower than the FET value.

The radial pin powers from the FET and C3 cases are presented in Figure 28, demonstrating excellent

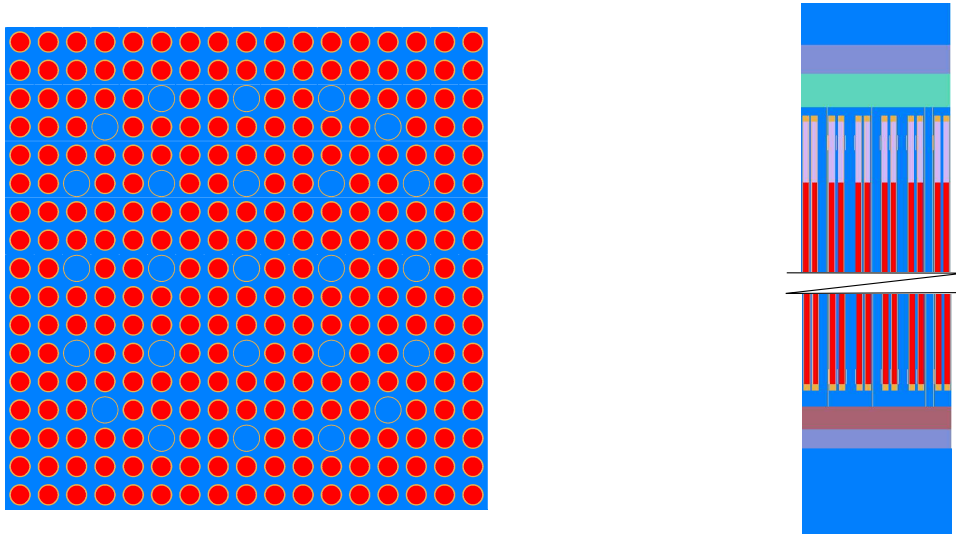


Figure 27. Radial (left) and axial (right) geometries of the three-dimensional assembly problem (not to scale).

	1.0374 1.0368 -0.06%	1.0378 1.0374 -0.04%		1.0369 1.0361 -0.08%	1.0328 1.0325 -0.03%		1.0117 1.0114 -0.03%	0.9770 0.9767 -0.03%	FET Case pin power C3 Case pin power Relative diff.
1.0370	1.0091	1.0093	1.0379	1.0091	1.0060	1.0267	0.9873	0.9718	
1.0360	1.0093	1.0091	1.0375	1.0086	1.0063	1.0271	0.9877	0.9722	
-0.10%	0.02%	-0.02%	-0.04%	-0.05%	0.03%	0.04%	0.04%	0.04%	
1.0381	1.0091	1.0106	1.0394	1.0113	1.0086	1.0282	0.9877	0.9723	
1.0374	1.0093	1.0101	1.0393	1.0106	1.0083	1.0274	0.9875	0.9719	
-0.07%	0.02%	-0.05%	-0.01%	-0.07%	-0.03%	-0.08%	-0.02%	-0.04%	
	1.0376	1.0397		1.0457	1.0453		1.0121	0.9741	
	1.0377	1.0387		1.0459	1.0457		1.0114	0.9739	
	0.00%	0.00%		0.00%	0.00%		0.00%	0.00%	
1.0371	1.0083	1.0111	1.0450	1.0318	1.0511	1.0365	0.9827	0.9649	
1.0368	1.0083	1.0117	1.0454	1.0320	1.0518	1.0361	0.9829	0.9642	
-0.03%	0.00%	0.06%	0.04%	0.02%	0.07%	-0.04%	0.02%	-0.07%	
1.0320	1.0058	1.0093	1.0457	1.0514		1.0175	0.9644	0.9556	
1.0337	1.0052	1.0084	1.0456	1.0517		1.0175	0.9647	0.9553	
0.16%	-0.06%	-0.09%	-0.01%	0.03%		0.00%	0.03%	-0.03%	
	1.0260	1.0276		1.0366	1.0173	0.9734	0.9480	0.9463	
	1.0267	1.0283		1.0363	1.0174	0.9733	0.9475	0.9462	
	0.07%	0.07%		-0.03%	0.01%	-0.01%	-0.05%	-0.01%	
1.0120	0.9878	0.9869	1.0115	0.9828	0.9649	0.9475	0.9381	0.9414	
1.0120	0.9880	0.9875	1.0117	0.9834	0.9650	0.9476	0.9382	0.9422	
0.00%	0.02%	0.06%	0.02%	0.06%	0.01%	0.01%	0.01%	0.08%	
0.9756	0.9717	0.9709	0.9733	0.9649	0.9556	0.9463	0.9417	0.9468	
0.9762	0.9720	0.9721	0.9737	0.9648	0.9553	0.9463	0.9413	0.9474	
0.06%	0.03%	0.12%	0.04%	-0.01%	-0.03%	0.00%	-0.04%	0.06%	

Figure 28. Pin powers from FET case are compared to case C3 for three-dimensional assembly problem.

agreement, with relative differences in pin powers being less than 0.2% across all fuel pins. Additionally, for the assembly problem, the FET case ran 1.6, 2.3, and 5.1 times faster compared to cases C1, C2, and C3, respectively. As previously mentioned, this significant computational speedup is partly due to the absence of localized strong neutron absorbers. In the next subsection, the computational time speedup will be evaluated for assembly problems containing strong neutron absorbers.

#### 4.2.4 Three-dimensional Assembly Problem with Neutron Absorbers

This test problem aims to evaluate the computational time speedup of the FET case for reactor problems with strong neutron absorbers. The presence of neutron absorbers is expected to reduce the efficiency of the rejection sampling in the delta-tracking method. The problem setup is identical to the assembly problem described in subsection 4.2.3, with the exception that either Pyrex or control rods are inserted into the guide tubes.

As previously described, the tip of the control rod is made from AIC, measuring 101.6 cm in length, while the remaining 259.05 cm is composed of boron carbide. In this problem, the control rod is inserted to a depth of 186 steps (where 1 step corresponds to 1.5875 cm), meaning only the AIC portion is inserted into the active core. This configuration makes the presence of the neutron absorber more localized, while the Pyrex burnable poisons occupy almost the entire active core axially.

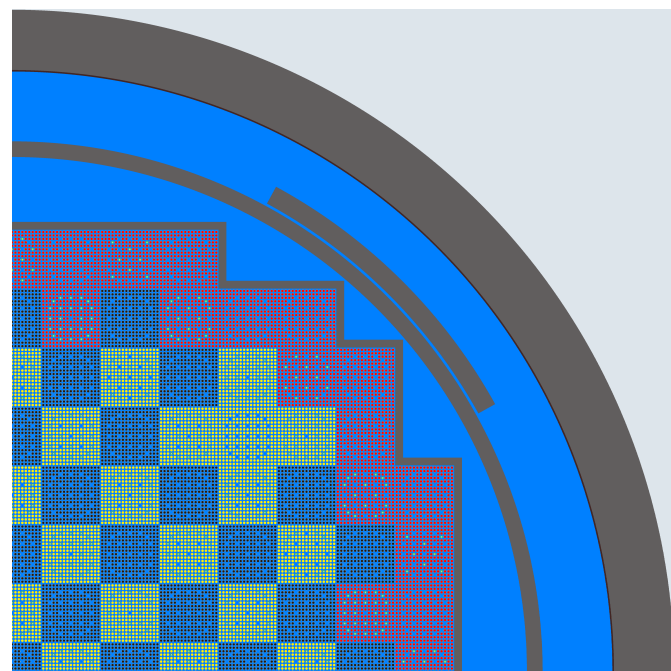
Table 7 provides  $k_{inf}$  solutions along with relative simulation times. As can be observed, the presence of Pyrex has little effect on the FET case speedup compared to problems without Pyrex, as shown in Table 6. This is because the presence of Pyrex is not localized, so the rejection sampling procedure in the delta-tracking can still be performed efficiently.

In contrast, the presence of control rods is very localized, located in a small portion at the top of the active core. This leads to poor rejection sampling efficiency in the delta-tracking method. As seen in Table 7, the FET speedup compared to a 100/5 axial/radial discretization with control rods inserted at 186 steps is 2.6 times. This speedup is much smaller than for problems without the control rods inserted, which is around 5.1 times, as observed in Table 6. The  $k_{inf}$  solutions generally follow the same trend as in previous problems, where they converge to the FET case solutions for infinitesimal cells.

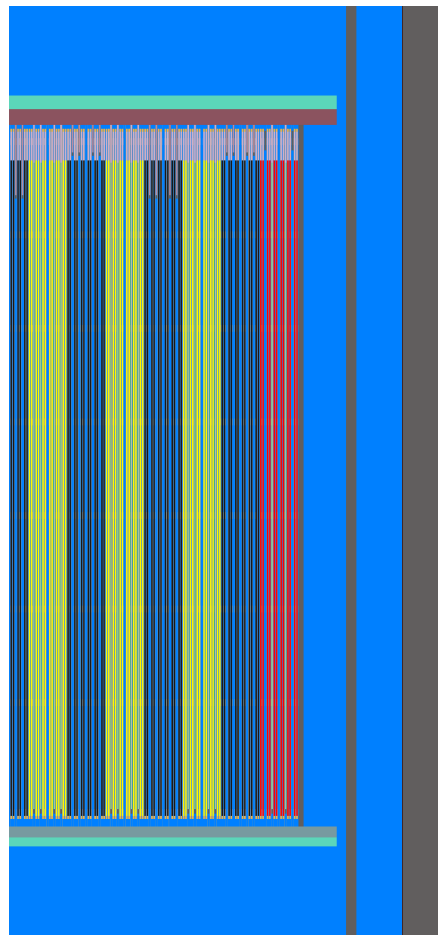
#### 4.2.5 Whole-core Reactor Problem

The final test problem for the spatially continuous material properties is a whole-core problem, based on Problem #7 of the VERA benchmark: a three-dimensional, beginning-of-cycle (BOC) physical reactor. This benchmark provides detailed descriptions of the reactor core geometry and internal structures. Figure 29 illustrates the detailed whole-core reactor geometry modeling of the VERA benchmark in MCS. This test problem estimates the CBC at HFP.

As with the previous test problems, several cases were developed to compare the spatially continuous material approach with the cell-based approach. These cases, along with descriptions of the cell discretizations, are listed in Table 8. Note that all simulations utilized  $6 \times 10^4$  particles per cycle, over a total of 37,500 cycles, with 30,000 cycles designated as active. This number of particle of histories



(a) Radial view.



(b) Axial view.

Figure 29. Detailed whole-core reactor geometry modelling in MCS.

Table 7. Calculation results for three-dimensional assembly problem with neutron absorbers.

Cases	# of fuel pellet axial/radial discretization	Pyrex		Control Rods	
		$k_{inf}$	Relative wall-clock time	$k_{inf}$	Relative wall-clock time
D1	25/1	$0.95876 \pm 0.00004$	1.5	$1.15972 \pm 0.00004$	0.8
D1	50/2	$0.95909 \pm 0.00004$	2.1	$1.16007 \pm 0.00004$	1.1
D2	100/5	$0.95918 \pm 0.00004$	4.7	$1.16027 \pm 0.00004$	2.6
FET	N/A	$0.95929 \pm 0.00004$	1.0 <sup>(a)</sup>	$1.16047 \pm 0.00004$	1.0 <sup>(b)</sup>

<sup>(a)</sup> The absolute wall-clock time for the FET case is 1.9 hours with 70 MPI processes.

<sup>(b)</sup> The absolute wall-clock time for the FET case is 3.5 hours with 70 MPI processes.

produces axially averaged pin-power densities with maximum standard deviation around 0.6%. In this problem, the reactor is modelled in a quarter core.

In the MCS modeling for the FET case, each fuel assembly has different delta-tracking region, with each assembly having its own majorant cross-section. Therefore, when a particle crosses an assembly surface, the particle track must be terminated. Subsequently, a new sampling of the distance to collision must be calculated using a different majorant cross-section. Additionally, the withdrawn RCCAs are excluded from the delta-tracking region to optimize the rejection sampling procedure. c Therefore, to improve performance, the withdrawn RCCAs are not included in the delta-tracking region in the FET case.

The CBC results are presented in Table 8. As shown in the table, the behavior of the solutions is similar to those from the previous problems, where the CBC from the cell-based converges to that from the FET case using spatially continuous material properties. The CBC difference, compared to the E1 case with 25/1 radial/axial cell discretizations, is around 7 ppm, corresponding to approximately 70 pcm of reactivity. This result is consistent with previous solutions. Moreover, the FET case only requires one-third of the simulation time to achieve similar or even better accuracy compared to the E2 case with 60/5 radial/axial cell discretizations.

In this whole-core problem, the random access memory (RAM) requirements were also evaluated. The memory usage was measured in the Ubuntu operating system using the `free -m` command during the simulation. As shown in the table, the FET case requires only 20% of the RAM compared to the E3 case. This reduction in memory usage is mainly due to the fewer number of cells employed in the FET case. Although there is additional memory needed to store the FET coefficients, the number of coefficients is too small to offset the overall memory reduction. This demonstrates that the use of spatially continuous materials with FET not only achieves better accuracy with less simulation time, but also requires lower memory usage.

Figure 30 shows the assembly power map and its comparison between the FET and E3 cases. As

Table 8. Calculation results for whole-core problem.

Cases	# of fuel pellet axial/radial discretization	CBC (ppm)	Relative wall-clock time	Relative memory usage
E1	25/1	$859.6 \pm 0.2$	1.2	1.1
E1	50/2	$863.0 \pm 0.2$	1.8	2.4
E2	60/5	$864.0 \pm 0.2$	2.9	4.9
FET	N/A	$866.2 \pm 0.2$	1.0 <sup>(a)</sup>	1.0 <sup>(b)</sup>

<sup>(a)</sup> The absolute wall-clock time for the FET case is 14.3 hours with 70 MPI processes.

<sup>(b)</sup> The absolute memory usage for the FET case is 146.4 GB per node, with each node running 35 MPI processes.

Table 9. Calculation results for FET cases utilizing different orders of Zernike and Legendre polynomials.

Zernike and Legendre order	CBC (ppm)	Relative wall-clock time	Relative memory usage
2 <sup>nd</sup>	$866.0 \pm 0.2$	0.90	0.70
4 <sup>th</sup>	$866.1 \pm 0.2$	0.93	0.80
6 <sup>th</sup>	$865.7 \pm 0.2$	0.97	0.90
8 <sup>th</sup>	$865.6 \pm 0.2$	1.00 <sup>(a)</sup>	1.00 <sup>(b)</sup>
10 <sup>th</sup>	$866.0 \pm 0.2$	1.03	1.10

<sup>(a)</sup> The absolute wall-clock time for the 8<sup>th</sup> order case is 14.5 hours with 70 MPI processes.

<sup>(b)</sup> The absolute memory usage for the 8<sup>th</sup> order case is 153.1 GB per node, with each node running 35 MPI processes.

observed, the maximum and minimum assembly power relative differences are approximately 0.3%, with a root mean squared error (RMS) of 0.2%. And the relative difference on axial power, shown in Figure 31, is also less than 1%. At the pin level, the normalized radial pin-power densities also exhibit good agreement between the FET and E3 cases, with an RMS of 0.3%, and maximum and minimum relative differences of less than 2%, as shown in Figure 32. Additionally, the three-dimensional view of radially pin-averaged coolant and fuel temperatures from FET case are plotted in Figure 33. These results confirm that the solutions with spatially continuous material properties are well aligned with the cell-based cases that use very small cells.

A set of FET cases utilizing various orders of Zernike and Legendre polynomials was conducted to assess the effects of polynomial order on accuracy, running time, and memory usage. The results for these cases are presented in Table 9. It should be noted that in Table 9, the Zernike and Legendre polynomials are of the same order for each case. Additionally, the running time and memory usage are calculated relative to the 8<sup>th</sup> order case.

As can be seen in Table 9, the solution accuracy for CBC is quite good even with the use of 2<sup>nd</sup>

						FET Case	E3 Case	Rel. Diff.
						Max. Diff	0.3%	
						Min. Diff	-0.3%	
						RMS	0.2%	
0.757	0.858	0.765	0.632					
0.757	0.858	0.766	0.632					
0.0%	0.0%	-0.1%	0.0%					
1.055	1.017	1.061	0.991	0.893	0.606			
1.054	1.017	1.062	0.992	0.895	0.607			
0.1%	0.0%	-0.2%	-0.2%	-0.3%	-0.2%			
1.055	1.159	1.124	1.124	0.867	0.868	0.606		
1.054	1.159	1.125	1.125	0.869	0.870	0.607		
0.1%	0.1%	-0.1%	-0.1%	-0.2%	-0.2%	-0.2%		
1.157	1.079	1.186	1.079	1.245	0.867	0.893		
1.155	1.077	1.186	1.080	1.245	0.869	0.895		
0.2%	0.1%	0.0%	-0.1%	-0.1%	-0.2%	-0.3%		
1.052	1.145	1.071	1.179	1.079	1.123	0.992	0.633	
1.050	1.142	1.070	1.181	1.080	1.124	0.991	0.631	
0.2%	0.2%	0.0%	-0.2%	-0.1%	-0.1%	0.1%	0.2%	
1.109	0.976	1.125	1.069	1.184	1.124	1.061	0.766	
1.106	0.974	1.125	1.070	1.186	1.124	1.060	0.763	
0.3%	0.2%	0.0%	-0.2%	-0.2%	0.0%	0.1%	0.3%	
1.022	1.101	0.975	1.142	1.076	1.158	1.016	0.859	
1.020	1.098	0.974	1.143	1.078	1.157	1.014	0.856	
0.3%	0.2%	0.0%	-0.1%	-0.1%	0.1%	0.2%	0.3%	
1.111	1.022	1.108	1.049	1.154	1.054	1.054	0.757	
1.107	1.020	1.107	1.050	1.156	1.053	1.051	0.755	
0.3%	0.2%	0.1%	0.0%	-0.2%	0.1%	0.3%	0.3%	

Figure 30. Assembly powers comparison between FET and E3 cases.

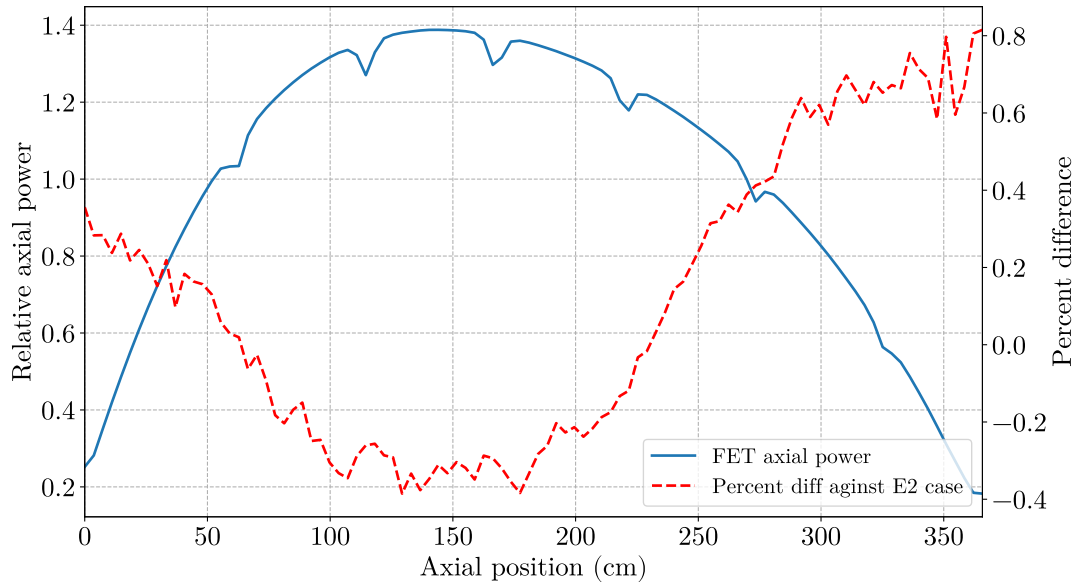


Figure 31. Axial power from FET case compared with that from E3 case for the whole-core problem.

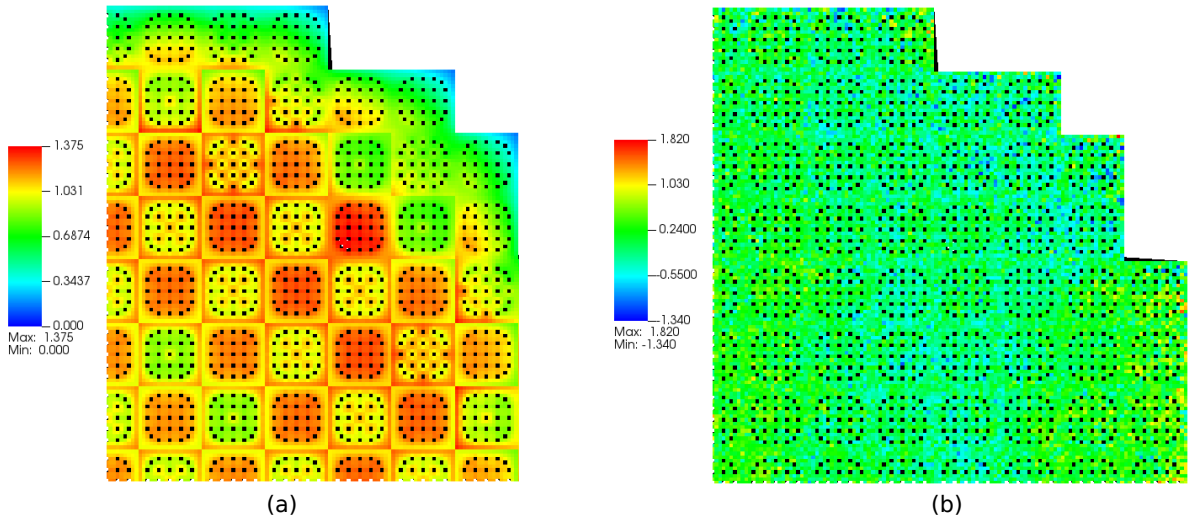


Figure 32. Normalized radial pin-power densities of the FET case for the whole-core problems (a), and their comparisons against E3 case (b).

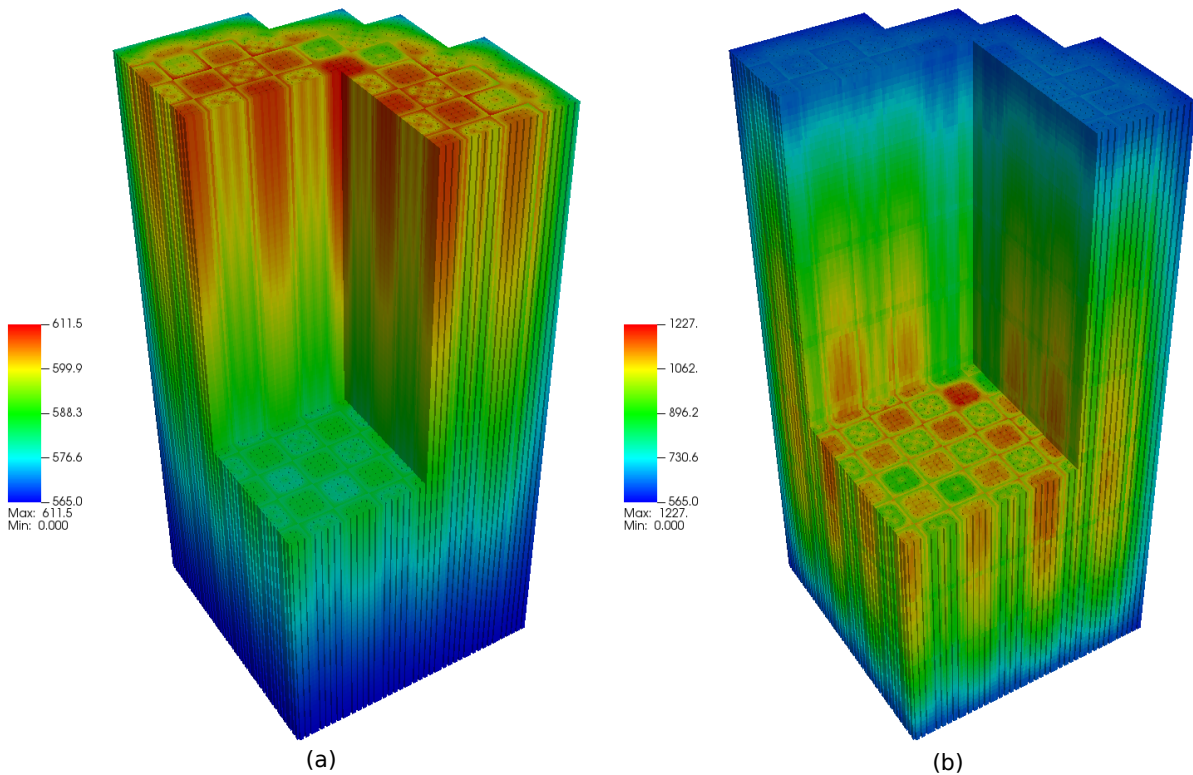


Figure 33. Three-dimensional view of radially pin-averaged coolant temperature (a) and fuel temperature (b) from FET case.

order Zernike and Legendre polynomials. The results for these 2<sup>nd</sup> order polynomials still fall within the statistical uncertainties for both CBC and power distribution, making it difficult to compare their accuracy. However, the use of low-order polynomials is generally not recommended for broader problems, as it may compromise calculation accuracy. Interesting observations can be made regarding how the polynomial order impacts running time and memory usage: an increase in polynomial order by two leads to a 3% increase in running time. Similarly, an increase in two polynomial order results in approximately a 10% rise in memory usage. Thus, it is evident that the polynomial order significantly affects memory usage during MC multi-physics coupled simulations that utilize spatially continuous material properties.

### 4.3 Thermal Expansion

To assess the effects of thermal expansion (TE) modeling on MC coupled multi-physics reactor simulations, a series of test problems were developed. These test problems include assembly and core problems, as well as depletion problems with restart cases. The problem geometries and material compositions were adopted from the Virtual Environment for Reactor Applications (VERA) core physics benchmark [35].

In all problems discussed in this subsection, the thermal-hydraulic (TH) parameters are updated every 500 cycles of MCS particle tracking. In MCS, the fuel pellets are axially discretized into 25 equidistant cells without radial discretization. Correspondingly, the TH solver also discretizes the active core axially into 25 equidistant meshes that align with the MCS cells. Additionally, in the TH solver, the fuel pellets are radially divided into 10 equidistant rings, whereas the cladding and gap are each represented by a single ring to numerically solve the heat conduction equation. The radial fuel temperature profile from TH solver is then averaged to obtain the radially-averaged fuel pellet temperature for use in MCS simulation.

#### 4.3.1 Small Lattice Problem

This small lattice problem consists of a  $2 \times 2$  pin cells with two different fuel enrichments: 3.1% wt. fuel enrichment in all fuel pins, except for the bottom-left pin, which has 2.1% wt. enrichment, as shown in Figure 34. The pin geometry and material compositions are based on the VERA benchmark, with a 0.4 cm inter-lattice gap. The boron concentration diluted in the coolant is 1300 ppm. This problem simulated  $4 \times 10^4$  particles per cycle, with a total of 14,500 cycles, of which 12,000 were designated as active cycles.

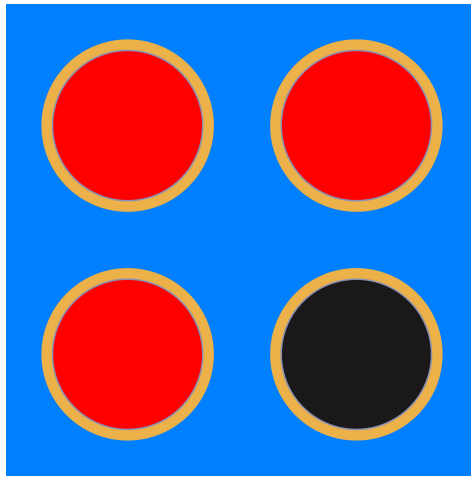


Figure 34. Small lattice problem geometry.

This simple problem is designed to evaluate the implementation of TE in the MC code MCS by comparing the solutions from on-the-fly TE in MCS to those from manually calculated TE. In the manual calculations, the geometrical expansions and expanded material densities were manually computed

Table 10. Small lattice problems infinite multiplication factors.

Cases	$k_{inf}$
On-the-fly TE	$1.14279 \pm 0.00003$
Manually calculated TE	$1.14272 \pm 0.00004$
No TE	$1.14364 \pm 0.00003$

based on the pin-averaged temperatures from the on-the-fly thermal expansion calculation results. Note that the varying fuel enrichments in this problem result in non-uniform pin-averaged temperatures. A new MCS input file was then created using these manually calculated geometrical expansions and expanded material densities to represent the equivalent TE.

Table 10 presents the results for small lattice problem. As observed, the on-the-fly TE and manually calculated TE produce very similar infinite multiplication factors, with only a 7 pcm difference, which is well within the given statistical uncertainty. For comparison, the result without TE is also given that shows a difference of more than 80 pcm compared to the TE cases. These results confirm that on-the-fly TE is correctly implemented in the MCS code.

### 4.3.2 Assembly Problem

This test problem aims to assess the effects of TE at the assembly level. It is based on a case similar to Problem 6 of the VERA benchmark. The problem geometry includes non-fuel structural components such as the pin plenum, nozzles, core plates, and top and bottom reflectors. The TE effects are analyzed for various boron concentrations and fuel enrichment levels, with the reactor set to Hot Full Power (HFP) conditions. Note that the calculations for this problem simulated  $4 \times 10^4$  particles per cycle, with a total of 14,500 cycles, of which 2,500 cycles were designated as active.

Tables 11 and 12 present the assembly reactivity differences caused by TE for varying boron concentrations and fuel enrichment levels, respectively. Table 11 demonstrates that as boron concentration increases, the reactivity difference decreases. This occurs because the moderator volume, which contains boron, expands due to an increase in pin pitch. With higher boron concentrations, the neutron absorption rate rises, resulting in a lower eigenvalue. Conversely, at lower boron concentrations, the improvement in neutron moderation offsets the increase in absorption rates and resulting a higher eigenvalue. It is well known that reactivity differences due to TE are strongly influenced by boron concentration in the reactor. Similarly, Table 12 shows that higher fuel enrichment levels lead to more positive reactivity differences due to TE. These trends in reactivity differences for varying boron concentrations and fuel temperatures are consistent with those observed in reference [12].

### 4.3.3 Whole-core Reactor Problem

The core problem specifications are similar to those of Problem 7 from the VERA benchmark; however, instead of determining the critical boron concentration, this problem calculates eigenvalues

Table 11. Assembly reactivity differences due to TE (TE - no TE) for various boron concentrations using 3.1% wt. enriched fuel.

Boron concentration (ppm)	Reactivity differences (pcm)
0	$182 \pm 6$
600	$43 \pm 5$
1300	$-76 \pm 6$

Table 12. Assembly reactivity differences due to TE (TE - no TE) for different fuel enrichment levels at a boron concentration of 600 ppm.

Fuel enrichment (% wt.)	Reactivity differences (pcm)
2.1	$-35 \pm 4$
3.1	$43 \pm 5$
4.4	$101 \pm 6$

using a fixed boron concentration of 860 ppm. The reactor operating condition is set at HFP.

The effects of TE on the core problem are evaluated at various expansion temperatures, as can be seen in Table 13. For the core-averaged case, the nominal core-averaged reactor temperature at HFP is applied, with fuel expansion set at 900 K, while coolant and cladding expansion are set at 583 K. The assembly-averaged case uses assembly-level averaged temperatures for geometry expansion within each assembly, while the pin-averaged case applies pin-level averaged temperatures for each pin cell. All cases simulated  $3 \times 10^5$  particles per cycle over a total of 42,000 cycles, with 38,000 active cycles, resulting in a maximum relative standard deviation of 0.8% for radial pin powers.

Table 13 compiles the results of the whole-core reactor problem. Pin-power errors were calculated relative to the pin-averaged case. As shown in the table, when thermal expansion is not considered, the eigenvalue is overestimated compared to the pin-averaged case, and the errors at the pin level are more pronounced. Using core-averaged nominal temperatures improves the eigenvalue, reducing the difference to less than 10 pcm compared to the pin-wise case and also lowering pin-power errors. Greater accuracy is achieved when assembly-level temperatures are used for expansion temperature, yielding only a 4 pcm eigenvalue difference and a 0.3% RMS pin error. The results indicate that as the spatial

Table 13. Whole-core problem eigenvalues and pin-power power errors.

Expansion temperature	Eigenvalue	Min. pin error (%)	Max. pin error (%)	RMS pin error (%)
Room temperature	$1.00046 \pm 0.00002$	-4.8	1.9	0.8
Core-averaged temperature	$1.00004 \pm 0.00002$	-2.1	1.8	0.5
Assembly-averaged temperature	$1.00001 \pm 0.00002$	-1.4	2.0	0.3
Pin-averaged temperature	$0.99997 \pm 0.00002$	Ref	Ref	Ref

Table 14. Calculated ITCs compared with the measured value.

Cases	ITC (pcm/ $^{\circ}$ F)
No TE	$-3.74 \pm 0.24$
TE	$-3.31 \pm 0.22$
Measurement	-2.17

resolution of expansion temperatures increases, both the eigenvalue and pin powers converge toward those of the pin-wise case.

Figure 35 presents the radial pin-power errors relative to the pin-averaged case. The case without thermal expansion underestimates pin powers at the core periphery by up to  $-4.8\%$ , while overestimating pin powers near the core center. The core-averaged case yields reasonably accurate pin powers but still exhibits some deviations. The assembly-averaged case produces pin-power solutions that closely align with the pin-averaged case. Additionally, it is notable that the pin-wise case's runtime is only 0.9% longer than the case without thermal expansion, indicating that incorporating on-the-fly thermal expansion introduces virtually no additional computational cost.

#### 4.3.4 Isothermal Temperature Coefficient

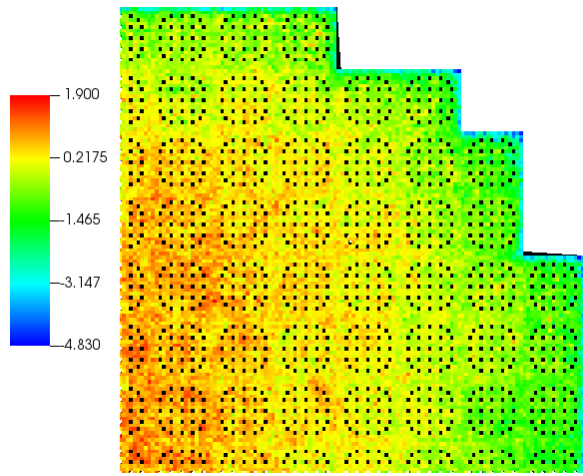
This test problems attempts to quantify the effect of thermal expansion on the isothermal temperature coefficient (ITC). The ITC represents the change in reactivity per unit change in fuel and moderator temperature [37]. ITC measurements are typically performed during Hot Zero Power (HZP) reactor physics tests to determine whether the measured ITC aligns with the calculated value [38].

In this study, the ITC measurement in the VERA benchmark was modeled for cases with and without TE. The reactor used in this benchmark is Watts Bar Unit 1, a Westinghouse PWR. The measured ITC was obtained during cycle 1, with all fresh fuel. The ITC was calculated using isothermal temperatures of 560 K and 570 K, with a boron concentration of 1291 ppm.

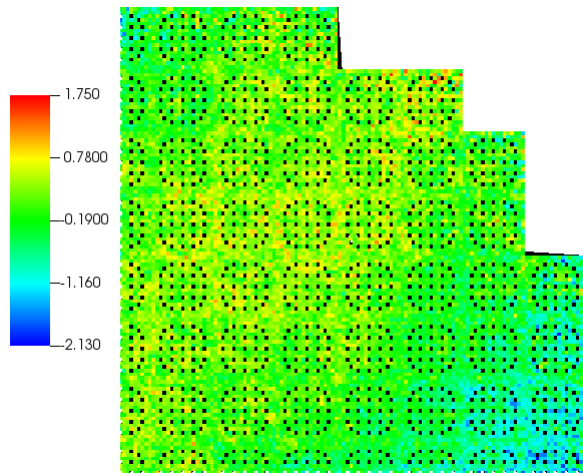
To ensure statistical reliability, the ITC mean and the corresponding standard deviations were obtained by performing five runs for each case, with random seeds for each run. This resulted in a total of 25 ITC samples, from which the mean and standard deviation were calculated. For each run, there were 14,500 cycles, of which 2,500 cycles were inactive, with  $4 \times 10^4$  particle histories simulated for every cycle.

The results are displayed and compared against measurement result in Table 14. As indicated in the table, incorporating TE into core modeling improves the accuracy of the ITC, bringing it closer to the measured data. Additionally, the results show that TE modeling makes the ITC more positive by 0.4 pcm/ $^{\circ}$ F. This difference is slightly higher than the findings in Palmtag et al. [12], which reported that TE modeling increases the ITC by 0.2-0.3 pcm/ $^{\circ}$ F.

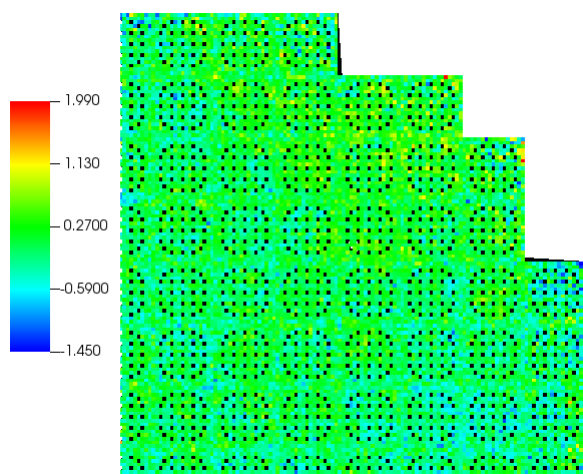
Although the ITC solutions for both the TE and No TE cases deviate significantly from the reported measured value, they are still comparable to the results of other MC calculations. For example, the ITC solution from KENO without TE is 3.18 pcm/ $^{\circ}$ F [35].



(a) No TE case.



(b) Core-averaged case.



(c) Assembly-averaged case.

Figure 35. Radial pin-power errors distributions relative to the pin-averaged for each case.

Table 15. Critical boron concentrations for depletion problem.

Cases	EFPDs	Percent power	Bank D step	Critical Boron Concentration (ppm)		
				Measurement	TE	No TE
BOC	0.0	0.0	186	1299	$1277 \pm 0.8$	$1286 \pm 0.6$
MOC	221.1	100.0	222	530	$485 \pm 0.9$	$474 \pm 0.8$
EOC	392.3	86.9	202	38	$35 \pm 0.9$	$11 \pm 0.7$

#### 4.3.5 Whole-core Reactor Depletion using Restart Calculations

Exercise 3 of the TVA Watts Bar Unit 1 multi-physics depletion benchmark [36] was adopted to investigate the effect of TE on the boron letdown curve during reactor depletion. Restart cases from whole-core pin-by-pin depletion without TE were run at 0.0, 221.1, and 392.3 effective full power days (EFPDs) for cases with and without TE. This depletion problem simulated  $6 \times 10^4$  particles per cycles, with a total of 5,000 cycles, of which 2,500 were active cycles.

MCS, coupled with the CTF thermal-hydraulics solver [33], was used to solve this problem. The work on MCS/CTF multi-physics coupling was done in the previous studies [39]. The results were compared against the measured values obtained from reference [35] and are presented in Table 15.

As shown in the table, direct core modeling with TE yields more accurate predictions for this depletion whole-core problem, particularly as power increases and fuel burnup progresses. At the beginning of the cycle (BOC), core modeling with TE underestimates the measured critical boron concentration (CBC) by 22 ppm, which is slightly higher than the 13-ppm underestimation observed with core modeling without TE. This higher CBC underestimation in the TE model at BOC is attributed to the high boron concentration and zero power at the start of the cycle. However, as the fuel cycle progresses and power increases, core modeling with TE offers more precise CBC solutions. For instance, at the end of the cycle (EOC), the TE model underestimates the CBC by just 3 ppm, compared to a 27-ppm underestimation by the model without TE. These results indicate that direct core modeling with TE provides more accurate solutions, particularly at full power and higher fuel burnup levels.

## 4.4 Combined Framework

In the preceding subsections, the multi-physics simulations with spatially continuous material and thermal expansion (TE) were tested individually. In this final subsection, the solutions to reactor multi-physics problems using combined spatially continuous material and thermal expansion methods will be presented and discussed. Two problems, assembly and whole-core multi-physics reactor problems, will be used to verify the implementation of combined framework.

The use of functional expansion tally (FET) in multi-physics simulations with spatially continuous material properties presents several challenges when combined with thermal expansion. Thermal expansion causes the fuel pellet radius and length to change during particle transport. Since FET also needs this information, the FET geometry information must be modified accordingly. Furthermore, during FET tally reconstruction, these geometric changes in the fuel pellet must also be considered to ensure accurate tally reproduction.

### 4.4.1 Assembly Problem

This problem is identical to the assembly problem in subsection 4.2.3, with similar modeling in MCS, except that thermal expansion is also modeled. Additionally, four cases have been developed in this problem, similar to those in subsection 4.2.3. This problem has 1300 ppm of boric acid diluted in the coolant. The calculation parameters employed for this problem are similar to those used in the previous assembly problem.

Table 16 presents the solutions for all cases, both with and without thermal expansion. It can be observed that, as in the previous problems, the solutions from cell-based cases converge to those from the FET cases as the cells become smaller. Moreover, due to the high concentration of boron diluted in the coolant, thermal expansion modeling reduces the  $k_{inf}$ , thereby countering the effects of spatially continuous material modeling.

It is important to note that the  $k_{inf}$  solution from MCS with thermal expansion modeling is very close to the solution from VERA-CS [40], which also modelled thermal expansion. The  $k_{inf}$  from VERA-CS is 1.16361. This corresponds to a 17 pcm difference compared to the FET case, or a 7 pcm difference compared to the F2 case with 100/5 discretization. These solutions demonstrate that the implementation of multi-physics simulations, which incorporate spatially continuous material properties and thermal expansion, is correct.

### 4.4.2 Whole-core Reactor Problem

This whole-core problem is similar to the one described in subsection 4.2.5, including the Calculation conditions, but it includes thermal expansion modeling. Additionally, four cases similar to those in subsection 4.2.5 have been developed for this problem.

Table 17 presents the CBC solutions for all cases. As expected, the CBC from cell-based cases converges to that from the FET case as the size of the cells decreases. As in the previous assembly problem,

Table 16. Calculation results for the assembly problem using combined framework.

Cases	# of fuel pellet axial/radial discretization	$k_{inf}$	
		No TE	TE
F1	25/1	$1.16400 \pm 0.00004$	$1.16321 \pm 0.00004$
F1	50/2	$1.16443 \pm 0.00004$	$1.16350 \pm 0.00004$
F2	100/5	$1.16449 \pm 0.00005$	$1.16368 \pm 0.00005$
FET	N/A	$1.16465 \pm 0.00004$	$1.16378 \pm 0.00004$

Table 17. Calculation results for the whole-core problem using combined framework. Critical boron search problem.

Cases	# of fuel pellet axial/radial discretization	CBC (ppm)	
		No TE	TE
G1	25/1	$859.6 \pm 0.2$	$855.7 \pm 0.2$
G1	50/2	$863.0 \pm 0.2$	$859.3 \pm 0.2$
G2	60/5	$864.0 \pm 0.2$	$859.9 \pm 0.2$
FET	N/A	$866.2 \pm 0.2$	$861.2 \pm 0.2$

the effect of thermal expansion in this problem counteracts the modeling with spatially continuous material properties. That is because, with around 800 ppm boron concentration, thermal expansion reduces the reactivity.

To more clearly observe the effects of thermal expansion, another whole-core problem is run with boron concentration set to zero. However, instead of estimating the critical boron concentration, this problem calculates the reactor eigenvalue. All other modeling parameters and cases are the same as those described in subsection 4.2.5.

Table 18 compiles all infinite multiplication factors from all cases both with and without thermal expansion. For reactor problems with zero boron concentration, the thermal expansion modelling adds the reactivity by around 120 pcm as can be observed in the Table 18. Also, as in the previous problems, the eigenvalue from cell-based cases converges to that from the FET case as the cells' size smaller.

Table 18. Calculation results for the whole-core problem using combined framework. Eigenvalue problem with 0 ppm of boron concentration.

Cases	# of fuel pellet axial/radial discretization	$k_{inf}$	
		No TE	TE
H1	25/1	$1.09655 \pm 0.00002$	$1.09789 \pm 0.00002$
H1	50/2	$1.09704 \pm 0.00002$	$1.09826 \pm 0.00002$
H2	60/5	$1.09717 \pm 0.00002$	$1.09839 \pm 0.00002$
FET	N/A	$1.09743 \pm 0.00004$	$1.09860 \pm 0.00004$

All these results demonstrate that the incorporation of multi-physics simulations with spatially continuous material properties and thermal expansion into reactor modeling can significantly enhance simulation fidelity. Therefore, the framework has the potential to be incorporated into future Monte Carlo production codes to meet the growing demands for improved reactor safety.

## V Conclusion

### 5.1 Thesis Summary

The primary objectives of this thesis were to investigate and develop a framework that enhance the fidelity of current Monte Carlo (MC) multi-physics coupling in reactor simulations by incorporating:

1. MC multi-physics coupling with spatially continuous material properties.
2. On-the-fly thermal expansion (TE) capabilities.

The introduction of MC multi-physics coupling with spatially continuous material properties was facilitated by the use of Functional Expansion Tallies (FET) and delta-tracking techniques. FET was employed to obtain continuous representations of power, which enables the calculation of nearly continuous material properties distributions such as temperature and density. Then by using spatial interpolation, material properties at any spatial points can be calculated. Meanwhile, delta-tracking was utilized as a particle tracking method in a continuous medium, overcoming the limitations posed by traditional surface tracking methods. These enhancements significantly reduce the need for spatial discretization commonly required in MC multi-physics reactor simulations, thereby preserving the advantages of the MC method in handling continuous geometry.

On-the-fly thermal expansion was integrated to address the challenge that the core temperature profile required for TE is not known *a priori* and is typically non-uniform across the core. By incorporating on-the-fly thermal expansion, the core geometry can be modified on-the-fly during particle tracking based on the local temperatures at the pin-level. This method more closely emulates natural phenomena and is expected to yield more accurate solutions.

Each of these approaches was tested individually on several reactor problems, ranging from pin to whole-core levels, to assess their applicability and advantages. The continuous representation of the intra-fuel pellet profile enabled by MC multi-physics coupling with spatially continuous material properties captures more precise resonance absorption at the fuel-pellet periphery. This leads to a more accurate eigenvalue solution from the proposed framework.

Additionally, incorporating spatially continuous material properties results in solutions that asymptotically converge to those obtained from conventional cell-based discretized simulations with infinitesimally small cells as observed in the two-dimensional pin-cell problem. Similar behavior is observed in three-dimensional pin cell and assembly problems, where the continuous representation of material properties yields more accurate solutions for both eigenvalue and axial power distributions, compared against the conventional cell-based discretization approach. In the whole-core reactor problem, the proposed approach reproduces high-fidelity solutions for both eigenvalue and pin powers, while accelerating the simulation time to almost three times faster and requiring 80% less memory than the cell-based discretization approach using very small cells.

The numerical test problems with on-the-fly thermal expansion demonstrate that the trends in reactivity differences due to thermal expansion for varying boron concentrations and fuel temperatures, as

well as the improvement in calculated ITC with thermal expansion, are consistent with previous studies. While using core-averaged temperatures for expansion is fairly accurate, employing local temperatures can enhance accuracy. Incorporating thermal expansion also improves the solutions for depletion problems, particularly at high power and high fuel burnup. This improvement is evident in the depletion problem using restart case, where modeling thermal expansion significantly improves the critical boron concentration (CBC) at the end of cycle (EOC).

In conclusion, this thesis has successfully demonstrated that the integration of MC multi-physics coupling with spatially continuous material properties and on-the-fly thermal expansion capabilities significantly enhances the accuracy and efficiency of reactor simulations.

## 5.2 Future Work

While the results of the proposed framework are promising, several enhancements are necessary to make the framework suitable for real reactor problems and to further optimize the proposed methods. Here are several recommended areas of development:

1. The most natural extension of this framework is the integration of continuous material depletion. Incorporating this feature along with fuel assembly shuffling capabilities would make the framework immediately applicable to real reactor problems. However, accurately representing the continuous radial profile of U-238 absorption rates remains challenging. The U-238 absorption rate is notably high at the periphery of the fuel pellet and decreases steeply towards the center due to spatial self-shielding. Unfortunately, such radial profiles cannot be adequately represented using FET with Zernike polynomials, as FETs are only suited for approximating smooth functions. Using piecewise function, as in the axial direction, is also not a solution because Zernike function is valid for a unit disk, not an annulus. Therefore, alternative polynomial functions, or perhaps completely different approach is necessary to obtain a continuous radial profile for U-238 absorption rates.
2. Using interpolation to determine material properties at any point might not be the best approach, particularly for fuel pellets where numerous interpolation points are required. The interpolation points for fuel pellet temperature and xenon distribution are two-dimensional in the radial and axial directions; thus they require more interpolation points, and in turn more memory. The memory requirement is compounded if continuous depletion is implemented, as the interpolation points for hundreds of nuclides' densities in each fuel pellet must also be saved during particle tracking. A potential solution could be to represent continuous fuel pellet temperature and nuclide densities using FET. However, this approach might also necessitate storing numerous FET coefficients, especially in the presences of spacer grids, where the material properties distributions must be represented using piecewise functions. Additionally, as previously mentioned, evaluating material properties at any point using FET requires more arithmetical operations than spatial interpolation. Therefore, the trade-offs associated with using FET to represent continuous material properties must be carefully studied.

These extensions are worth exploring to enhance the practical utility of this framework, enabling it to solve real reactor problems with greater accuracy and improved fidelity through more reasonable simulations. This progress will be instrumental in optimizing reactor design and operation, ensuring safer and more efficient nuclear energy production.

## References

- [1] T. D. C. Nguyen, H. Lee, S. Choi, and D. Lee, “MCS/TH1D analysis of VERA whole-core multi-cycle depletion problems,” *Annals of Nuclear Energy*, vol. 139, May 2020.
- [2] D. J. Kelly, A. E. Kelly, B. N. Aviles, A. T. Godfrey, R. K. Salko, and B. S. Collins, “MC21/CTF and VERA multiphysics solutions to VERA core physics benchmark progression problems 6 and 7,” *Nuclear Engineering and Technology*, vol. 49, no. 6, pp. 1326–1338, Sep. 2017.
- [3] Y. Ma, S. Liu, Z. Luo, S. Huang, K. Li, K. Wang, G. Yu, and H. Yu, “RMC/CTF multiphysics solutions to VERA core physics benchmark problem 9,” *Annals of Nuclear Energy*, vol. 133, pp. 837–852, Nov. 2019.
- [4] K. Smith and B. Forget, “Challenges in the Development of High-Fidelity LWR Core Neutronics Tools,” in *International Conference on Mathematics and Computational Methods Applied to Nuclear Science and Engineering (M&C 2013)*, Sun Valley, ID, May 2013.
- [5] N. Choi and H. G. Joo, “Analytic treatment of intra-fuel-rod temperature distributions in the GPU-based continuous energy Monte Carlo code PRAGMA,” in *Transactions of the American Nuclear Society Annual Meeting*, 2020.
- [6] J. Leppänen, “Modeling of nonuniform density distributions in the serpent 2 monte carlo code,” *Nuclear Science and Engineering*, vol. 174, no. 3, pp. 318–325, 2013.
- [7] M. S. Ellis, “Methods for including multiphysics feedback in Monte Carlo reactor physics calculations,” Thesis, Massachusetts Institute of Technology, 2017.
- [8] W. L. Chadsey, C. W. Wilson, V. W. Pine, W. L. Chadsey, C. W. Wilson, and V. W. Pine, “X-ray photoemission calculations,” *IEEE Transactions on Nuclear Science*, vol. 22, no. 6, pp. 2345–2350, Dec. 1975.
- [9] D. Griesheimer, “Functional expansion tallies for Monte Carlo simulations,” Ph.D. dissertation, University of Michigan, 2005.
- [10] F. B. Brown and W. R. Martin, “Direct sampling of Monte Carlo flight paths in media with continuously varying cross-sections,” in *Proc. ANS Mathematics & Computation Topical Meeting*, vol. 2, 2003.

- [11] B. Honarvar Shakibaei and R. Paramesran, “Recursive formula to compute Zernike radial polynomials,” *Optics Letters*, vol. 38, no. 14, p. 2487, Jul. 2013.
- [12] S. Palmtag, B. Kochunas, D. Jabaay, Z. Han, and T. Downar, “Modeling Thermal Expansion in VERA-CS,” in *Proceeding of International Conference on Mathematics & Computational Methods (M&C 2017)*, Jeju, South Korea, 2017.
- [13] K. Li, N. An, H. Luo, S. Huang, and K. Wang, “A better hash method for high-fidelity Monte Carlo simulations on nuclear reactors,” *Frontiers in Energy Research*, vol. 11, 2023.
- [14] C. Fiorina, S. Radman, M. Koc, and A. Pautz, “Detailed modelling of expansion reactivity feedback in fast reactors using OpenFOAM,” in *International conference on mathematics and computational methods applied to nuclear science and engineering (M&C 2019)*, Portland, OR, 2019, pp. 1434–1442.
- [15] Y. Ma, W. Han, B. Xie, H. Yu, M. Liu, X. He, S. Huang, Y. Liu, and X. Chai, “Coupled neutronic, thermal-mechanical and heat pipe analysis of a heat pipe cooled reactor,” *Nuclear Engineering and Design*, vol. 384, p. 111473, 2021.
- [16] Y. Guo, Z. Li, S. Huang, M. Liu, and K. Wang, “A new neutronics-thermal-mechanics multi-physics coupling method for heat pipe cooled reactor based on RMC and OpenFOAM,” *Progress in Nuclear Energy*, vol. 139, p. 103842, 2021.
- [17] M. M. Cole, C.-S. Lin, and J. Ortensi, “NRC Multiphysics Analysis Capability Deployment FY 2021 - Part 2,” Idaho National Laboratory, Tech. Rep. INL/EXT-21-62522, 2021.
- [18] C. J. Permann, D. R. Gaston, D. Andrš, R. W. Carlsen, F. Kong, A. D. Lindsay, J. M. Miller, J. W. Peterson, A. E. Slaughter, R. H. Stogner, and R. C. Martineau, “MOOSE: Enabling massively parallel multiphysics simulation,” *SoftwareX*, vol. 11, p. 100430, 2020.
- [19] M. Imron and D. Lee, “Monte carlo coupled multi-physics with spatially continuous material properties,” *Annals of Nuclear Energy*, vol. 210, p. 110856, 2025.
- [20] ——, “On-the-fly thermal expansion for monte carlo multi-physics reactor simulations,” *Frontiers in Nuclear Engineering*, vol. 3, p. 1483520, 2024.
- [21] H. Lee, W. Kim, P. Zhang, M. Lemaire, A. Khassenov, J. Yu, Y. Jo, J. Park, and D. Lee, “MCS – A Monte Carlo particle transport code for large-scale power reactor analysis,” *Annals of Nuclear Energy*, vol. 139, p. 107276, May 2020.
- [22] H. Lee, W. Kim, P. Zhang, A. Khassenov, J. Park, J. Yu, S. Choi, H. S. Lee, and D. Lee, “Preliminary simulation results of BEAVRS three-dimensional Cycle 1 whole core depletion by UNIST Monte Carlo code MCS,” in *Proceeding of International Conference on Mathematics & Computational Methods (M&C 2017)*, Jeju, South Korea, 2017.

- [23] J. Yu, H. Lee, M. Lemaire, H. Kim, P. Zhang, and D. Lee, “MCS based neutronics/thermal-hydraulics/fuel-performance coupling with CTF and FRAPCON,” *Computer Physics Communications*, vol. 238, pp. 1–18, 2019.
- [24] J. Yu, H. Lee, H. Kim, P. Zhang, and D. Lee, “Simulations of BEAVRS benchmark cycle 2 depletion with MCS/CTF coupling system,” *Nuclear Engineering and Technology*, vol. 52, no. 4, pp. 661–673, 2020.
- [25] J. Y. Wang and D. E. Silva, “Wave-front interpretation with zernike polynomials,” *Appl. Opt.*, vol. 19, no. 9, pp. 1510–1518, May 1980.
- [26] S. Hamilton, K. Clarno, B. Philip, M. Berrill, R. Sampath, and S. Allu, “Integrated radiation transport and nuclear fuel performance for assembly-level simulations,” in *PHYSOR 2012*, Knoxville, TN, April 2012.
- [27] J. Leppänen, “On the use of delta-tracking and the collision flux estimator in the Serpent 2 Monte Carlo particle transport code,” *Annals of Nuclear Energy*, vol. 105, pp. 161–167, 2017.
- [28] E. Woodcock, T. Murphy, P. Hemmings, and S. Longworth, “Techniques used in the GEM code for Monte Carlo neutronics calculations in reactors and other systems of complex geometry,” in *Proc. Conf. Applications of Computing Methods to Reactor Problems*, vol. 557. Argonne National Laboratory, 1965, issue: 2.
- [29] J. Leppänen, “Performance of Woodcock delta-tracking in lattice physics applications using the Serpent Monte Carlo reactor physics burnup calculation code,” *Annals of Nuclear Energy*, vol. 37, no. 5, pp. 715–722, 2010.
- [30] M. S. Ellis, C. Josey, B. Forget, and K. Smith, “Spatially Continuous Depletion Algorithm for Monte Carlo Simulations,” in *Transactions of the American Nuclear Society*, vol. 1. American Nuclear Society, 2016, pp. 1221–1224.
- [31] S. Choi, W. Kim, J. Choe, W. Lee, H. Kim, B. Ebironjumi, E. Jeong, K. Kim, D. Yun, H. Lee, and D. Lee, “Development of high-fidelity neutron transport code STREAM,” *Computer Physics Communications*, vol. 264, p. 107915, 2021.
- [32] M. Ryu, Y. S. Jung, H. H. Cho, and H. G. Joo, “Solution of the BEAVRS benchmark using the nTRACER direct whole core calculation code,” *Journal of Nuclear Science and Technology*, vol. 52, no. 7-8, pp. 961–969, Aug. 2015.
- [33] R. K. Salko, T. Lange, V. Kucukboyaci, Y. Sung, S. Palmtag, J. Gehin, and M. Avramova, “Development of COBRA-TF for modeling full-core, reactor operating cycles,” in *5th Topical Meeting on Advances in Nuclear Fuel Management, ANFM 2015*. American Nuclear Society, 2015, pp. 178–194.

- [34] J. Yu, H. Lee, H. Kim, P. Zhang, and D. Lee, “Preliminary coupling of the Thermal/Hydraulic solvers in the Monte Carlo code MCS for practical LWR analysis,” *Annals of Nuclear Energy*, vol. 118, pp. 317–335, 2018.
- [35] A. T. Godfrey, “VERA core physics benchmark progression problem specifications,” U.S. Department of Energy, Tech. Rep. CASL-U-2012- 0131-004, 2014.
- [36] T. Albagami, P. Rouxelin, A. Abarca, D. Holler, L. Moloko, M. Avramova, K. Ivanov, A. Godfrey, and S. Palmtag, “TVA Watts Bar Unit 1 Multi-Physics Multi- Cycle Depletion Benchmark Version 2.2,” OECD Nuclear Energy Agency, Tech. Rep. NEA/EGMPEBV/DOC(2020), 2021.
- [37] ANSI/ANS-19.6.1-2005, “Reload Startup Physics Tests for Pressurized Water Reactors,” American Nuclear Society, Tech. Rep., 2005.
- [38] S.-K. Hong, “Advanced On-Line Isothermal Temperature Coefficient Measurement for A Physics Test,” in *Transactions of the Korean Nuclear Society Autumn Meeting*, Jeju, South Korea, 2010, pp. 135–136.
- [39] J. Yu, H. Lee, H. Kim, P. Zhang, and D. Lee, “Preliminary validation of MCS multi-physics coupling capability with CTF,” in *Proceedings of the Reactor Physics Asia 2017 (RPHA17) Conference*, Chengdu, China, 2017.
- [40] M. Sieger, R. K. Salko Jr, B. Kochunas, B. Adams, and R. Williamson, “Vera 3.3 release notes,” CASL Technical Report: CASL-U-2015-0042-000, Tech. Rep., 2015.

## Acknowledgements

First and foremost, I am deeply grateful to Allah Almighty for His endless mercy and blessings throughout this journey. His grace has given me strength through all the challenges.

I would like to express my sincere thanks to my advisor, Prof. Deokjung Lee, for his invaluable advice, continuous encouragement, and financial support during my study in the CORE Laboratory. I am deeply grateful for the opportunity he provided me to study in his laboratory. Studying and working in the CORE Laboratory has opened new horizons of knowledge for me.

I also want to extend my appreciation to the members of my dissertation committee. Their thoughtful feedback and constructive criticism have greatly helped in refining my work and pushing me to achieve better results. My gratitude also extends to the staff at the Department of Nuclear Engineering at Ulsan National Institute of Science and Technology (UNIST).

I am also grateful to all my lab mates for their friendship, insightful discussions, and moral support. Their companionship has been a source of strength during tough times and has made the long hours in the lab much more enjoyable.

To my beloved parents, I cannot thank you enough. Your unconditional love, support, and prayers have been my constant source of motivation. Your sacrifices and unwavering belief in me are beyond words, and I dedicate this achievement to you.

Finally, I want to thank my family, especially my dear wife. Her love, patience, and strength have been my greatest support throughout this journey. She took care of our four sons while living abroad with me during my studies, and her dedication and sacrifice have made this accomplishment possible.

I would also like to express my thanks to everyone who has supported me in any way during this journey. Your help and encouragement have meant the world to me.

During the preparation of this thesis, the author used ChatGPT-4o and ChatGPT-4 to improve readability, clarity, and conciseness of the writing. After using this tool, the author reviewed and edited the content as needed.

